Mixing driven by transient buoyancy flows. Part 1. Kinematics

W.M.B. Duval[1], H. Zhong[2], C. Batur[3]

[1,a)]*Fluid Physics and Transport Processes Branch, NASA Glenn Research Center, Cleveland, Ohio 44135, USA*

[2]*Brookhaven National Laboratory, StonyBrook, New York 11973, USA*

[3]*Department of Mechanical Engineering, University of Akron, Akron, Ohio 44325-3903, USA*

Mixing of two miscible liquids juxtaposed inside a cavity initially separated by a divider, whose buoyancy-driven motion is initiated via impulsive perturbation of divider motion that can generate the Richtmyer-Meshkov instability, is investigated experimentally. The measured Lagrangian history of interface motion that contains the continuum mechanics of mixing shows self-similar nearly Gaussian length stretch distribution for wide range of control parameters encompassing approximate Hele-Shaw cell to three-dimensional cavity. Because of initial configuration of interface which is parallel to the gravitational field, we show that at critical initial potential energy mixing occurs through stretching of the interface, that shows frontogenesis, and folding owing to an overturning motion that results in unstable density stratification and produces an ideal condition for growth of single wavelength Rayleigh-Taylor instability. The initial perturbation of the interface and flow field generate Kelvin-Helmholtz instability and causes kinks at the interface, which grow into deep fingers during overturning motion and unfold into local whorl structures that merge and self-organize into the Rayleigh-Taylor morphology (RTM) structure. For a range of parametric space that yields two-dimensional flows, the unfolding of the instability through a supercritical bifurcation yields an asymmetric pairwise structure exhibiting smooth RTM that transitions to RTM fronts with fractal structures that contain small length scales for increasing Peclet number. The late stage of the RTM structure unfolds into an internal breakwave that breaks-down through wall and internal collision, and sets up the condition for self-induced sloshing that decays exponentially as the two fluids become stably stratified with a diffusive region indicating local molecular diffusion.

I. INTRODUCTION

Mixing driven by buoyancy-induced flows has wide applications to transport phenomena in materials processing for both terrestrial and the microgravity environment of the International Space Station (ISS). The control of the body force on ISS using vibration platforms allows accessibility to a much wider range of control parameters and in particular affects the intensity of flow fields. For example, the reduction of flow field intensity in microgravity allows uniform concentration gradient near phase interface in crystal growth processes such as solution,[1] directional solidification[2], and physical vapor transport[3] for technological applications. The uniformity of the concentration gradient is a desirable characteristic since it affects crystalline quality, however the coupling of the density field to concentration and or temperature can drive intense convective flows, which makes the ideal concentration profile prohibitive. Since the flow field is driven by the buoyancy force, of central importance to these problems is how buoyancy-driven flows stretch and fold an interface. We introduce an experiment to shed light into mixing driven by the buoyancy force.

a) Author to whom correspondence should be addressed. Electronic mail: walter.m.duval@nasa.gov

The need to address the effects of convection on concentration gradients in solution crystal growth of organic materials[4] conducted in microgravity experiments prompted ground-based experiments[5] on mixing driven buoyancy-induced flows between two liquids inside rectangular compartments separated by a barrier consisting of channels. These experiments[5] were carried out to investigate effects of convection on mass diffusion in order to shed light on the findings in Ref. 4. The complexity of the channel barrier[5] separating the two liquids, does not give direct access to interface information. The present experiment considers an ideal barrier design that allows the central question, as to how buoyancy-driven flows advect the interface between two miscible liquids, to be addressed in relation to computational findings in Ref. 6.

The computational experiments[6] predict the occurrence of a symmetric pairwise Rayleigh-Taylor morphology (RTM) structure due to the Rayleigh-Taylor instability mechanism for an ideal initial condition, while the physical experiments consider non-ideal initial condition and seeks to determine how the ideal initial condition of the computational model that yields symmetry can be approached. Symmetric structures, from the viewpoint of mixing have been used to drive more efficient mixing[7]. The experiments considered are implemented in search of a symmetric short-lived coherent structure such as RTM; we show that finding this symmetric structure remains an ideal goal that can be approached and presents a challenge to experimentalists. However the computational model[6] shows the basic features that are also observed experimentally, such as the distinct stages of development of the RTM structure. The early stages of RTM[6] have been shown to unfold from an overturning motion that generates a long wavelength Rayleigh-Taylor instability; the RTM structure takes several configurations with respect to a horizontal interface that depends on the initial potential energy of the system. The late stages[6] of the RTM structure unfold into an internal breakwave that breaks-down through wall and internal collision, and sets up the condition for self-induced sloshing that decays exponentially as the two fluids become stably stratified with a diffusive region indicating local molecular diffusion; since these features are robust they also observed experimentally.

Mixing is inherently a transient process involving initial segregation of two or more constituents, such as two liquids, and stirring in order to obtain uniformity or homogeneity[8]. Complex patterns emerge and dissipate between the two limits of segregation and homogeneity. Mixing occurs in a wide range of applications involving various mechanism of stirring including: convection in the Earth's mantle[9], convection of passive tracers in laminar flows due to energy injection from moving boundaries[10-14], large scale vortical structures sustained by shear flow[15,16], combustion processes[17], and mixing that occurs in the ocean[18-22] and atmospheric flows[23-25].

There exists a class of mixing flows for which the body force can be caused by deterministic acceleration, as well as random (stochastic) acceleration known as g-jitter. When the body force is parallel to the interface the effect of deterministic[26-28] and stochastic acceleration components[29,30] of the body force lends insight into effects of g-jitter on mixing driven by buoyancy-induced flows in a microgravity environment. Flows due to gravitational instability for which the body force is steady and perpendicular to the interface have been used as a basis to address mixing due to the Rayleigh-Taylor instability mechanism[31-37]. In our case we consider buoyancy-driven mixing in which the body force is steady and parallel to the interface initially. Mixing, sometimes used interchangeably with stirring, according to Ref. 38 consists of stretching and folding of material lines or surfaces and distribution throughout space with simultaneous diffusion of species and

This manuscript was accepted by Phys. Fluids. Click here to see the version of record.

energy. The flow field generates stretching and folding of the material line or surface. Our paradigm for buoyancy-driven mixing, with applications to crystal growth processes, consists of a flow field generated by the buoyancy force that redistributes a pseudo-material interface in which molecular mass diffusion is admitted. The experimental model contains the basic elements of mixing, stretching and folding of an interface caused by a flow field as well as molecular diffusion.

Related to the present experiment is the study of mixing due to Rayleigh-Taylor (RT) instability[31-37] which spans a range of initial perturbation from long to short wavelengths; the short wavelength initial perturbation can lead to turbulent mixing. For the RT instability problem, it has been shown in Ref. 39 that the deviation of the interface from planarity corresponds to a long wavelength one-half sawtooth initial perturbation, from adding a small angle of tilt $55' \leq \theta \leq 3°21'$ to the reference configuration. The addition of a small angle of tilt superimposed a two-dimensional motion on the structure of the perturbed interface which stretched the interface and contracted its mid-section. The mixing width of the interface decreased in comparison to the zero tilt angle RT instability; this was attributed to the stretching effect introduced via the initial tilt[39]. Our model experiment can be viewed as an extension of the tilt angle to 90° for reverse or backward flow and 270° for forward flow.

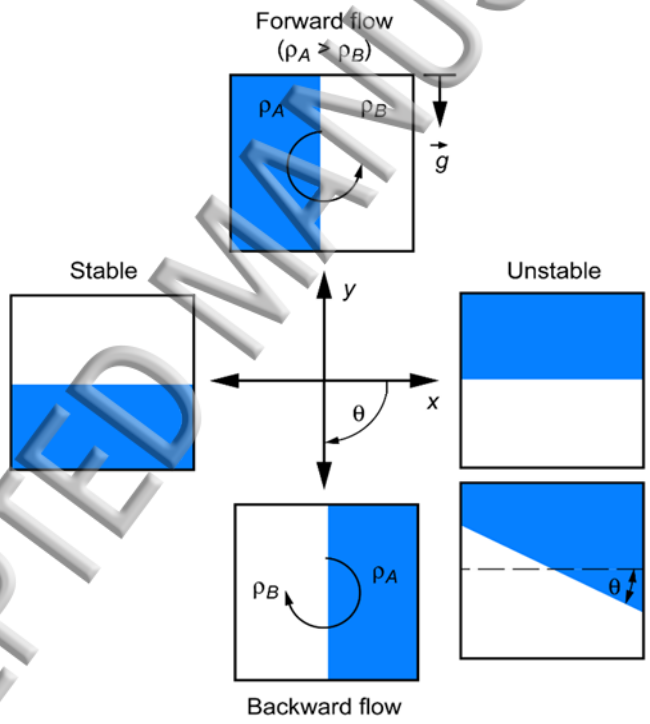

FIG. 1. Interface configuration between two fluids for a cycle of the tilt angle $0 \leq \theta \leq 2\pi$ with respect to the gravitational field.

A variation of tilt angle from $0 \text{ to } 2\pi$, the Rayleigh-Taylor perturbation cycle, corresponds to various configuration of the interface with respect to the gravitational field as shown in Fig. 1. In contrast to tilted interfaces, flat interfaces correspond to $\theta = n\pi/2$ with $n = 0,1,..4$; if the reference configuration of $\theta = 0$ is taken as the RT instability configuration for which the heavier

fluid overlays the lighter fluid initially, then $\theta = \pi$ corresponds to the stably stratified configuration. Owing to the sharp jump of density across the interface the unstable configuration $\theta = 0,\ 2\pi$ may be characterized as a square wave or step function initial perturbation. Two other step function initial perturbations exist at $\theta = \pi/2$ and $\theta = 3\pi/2$; however, the interface is parallel to the gravitational field. The configurations of $\theta = \pi/2,\ 3\pi/2$ have been used experimentally to investigate frontogenesis[40-42] due to gravity currents in lock-exchange flows that used a barrier to establish the initial condition. The remaining configurations in the RT instability cycle indicate variations of various sawtooth initial perturbations. In this context, our model experiment may be seen within a broader perspective of tilted RT problems. As shown in Fig. 1, all flows with initial conditions within the range of $0 \le \theta \le 2\pi$ lead to stable stratification for $\theta = \pi$ as a final configuration once transient effects decay. The stable stratification configuration has been used in Ref. 43 to address buoyancy-driven instability generated by chemical reaction at the interface between two reactant solutions, encompassing the Belousov-Zhabotinsky reaction[44] in closed and unstirred reactors, which show that reactant solutions with small density difference yield chemo-hydrodynamic patterns that are asymmetric[43] with respect to the initial contact line when chemical reaction occurs, and symmetric in absence of chemical reaction.

Within the framework of addressing buoyancy-driven mixing due to steady body force, we consider two miscible viscous liquids juxtaposed vertically inside a cavity where the orientation of the interface is parallel to the body force as in the forward flow with $\theta = 3\pi/2$ in Fig. 1. The effect of unsteady body force on mixing has applications to the study of the effect of induced vibration on transport processes in a microgravity environment[45]. Owing to the initial configuration with $\theta = 3\pi/2$ of our experiments, a divider is needed to separate the liquids initially between the two compartments of the cavity in order to establish the proper initial condition. In a microgravity environment, whereby the body force is reduced one million-fold, it is possible to remove the divider and establish the ideal initial condition of two fluids in intimate contact at an interface[45]. However, in this mechanical equilibrium state the two fluids would simply diffuse while remaining stationary and this would preclude the study of the mechanism of mixing such as stretching and folding of the interface.

In ground-based laboratory condition, by virtue of jump conditions across the interface due to pressure gradient and density gradient, impending motion occurs which stretches and folds the interface, from baroclinic vorticity generation. Since we cannot establish the ideal initial condition of undisturbed contact between the two fluids initially that would yield symmetry of the folding structure, we approximate this ideal condition through the impulsive velocity perturbation of divider motion between the two liquids over a range of pulling velocities or injected kinetic energy; this approximate initial condition introduces asymmetry in the system. One issue that we seek to resolve is the condition that symmetry is approached in our system, since it can potentially lead to more effective mixing. We show that the effect of high impulsive velocity perturbation at the interface, is analogous to shock-driven instability in compressible flow and shock-induced impulsive acceleration in incompressible nonhomogeneous liquids, and generates short time Richtmyer-Meshkov instability for certain range of parameters. This occurs through the basic mechanism of baroclinic vorticity generation at the interface resulting from interaction of the pressure gradient and density gradient across the interface.

The transient mixing characteristics of two liquids inside a cavity is addressed by measuring the Lagrangian history of the interface in Part 1 and the Eulerian flow field velocity using particle image velocimetry (PIV) in Part 2. The Lagrangian history is determined using a full-field view (FFV) photographic method to obtain a global view of the interface and planar laser-induced fluorescence (PLIF) to provide a local view for resolving the local details of a mid-plane section. The measurement of the flow field velocity is important in terms of understanding interface motion, since the flow field governs mixing of the interface. The problem is inherently transient and can also be three-dimensional for certain range of parameters, one issue of interest is the parametric region for which the problem can be well approximated as two-dimensional; this would allow insight to be drawn from the transient two-dimensional computational model[6]. To address this issue, we consider a cavity with a square cross-section 5 x 5 cm whose depth varies from 0.2 to 5 cm. This variation in depth spans an approximate two-dimensional Hele-Shaw cell to a three-dimensional cavity. The Hele-Shaw cell configuration has been used advantageously in various problems[46,47], to render the third dimension negligible thus reducing the problem to two-dimensions.

In the following sections, we introduce the experimental system in Sec. II. In Sec. III, we describe the experimental model and provide a description of mixing from which we deduce the parametric space and the descriptors of mixing such as its length stretch, interface width, and mixing efficiency. In Sec IV, we describe the experimental results and contrast the global view of the interface using FFV and its local view using PLIF. In Sec. V, we quantify the kinematics of interface motion from measurements of its length stretch, interface width, mixing efficiency, and its sloshing characteristic such as its damped natural frequency. In Sec. VI, we describe the local bifurcation of the interface as a function of the control parameters —Grashof or Peclet number, aspect ratio, and impulsive Reynolds number— from which we deduce a scaling law for the maximum length stretch. We summarize and conclude our findings in Sec. VII.

II. EXPERIMENTAL SYSTEM

Mixing driven by buoyancy-induced flows is characterized by measuring three primary metrics of the system: (a) the Lagrangian history of the interface length stretch $\mathcal{L}(t)$ and (b) its interface width $\delta w(t)$, using FFV method for a global view and PLIF for a local view of a plane cross-section in Part 1; and (c) the transient dynamics of the flow field $\vec{V}(\vec{x},t)$ using PIV in Part 2. The experimental system used to measure two of the metrics of the system is illustrated in Fig. 13 of Appendix A. We use two different light sources to quantify interface motion, integrating sphere for the FFV method and a planar laser sheet using a pulsed laser for the PLIF method. The description of the components used for interface tracking using FFV, and PLIF, are delineated in Appendix A.

III. DESCRIPTION OF EXPERIMENTAL MODEL

The physical description of the experimental model in Fig. 2 shows two viscous miscible liquids inside an enclosure with an initially prescribed density $\rho_A \geq \rho_B$ subjected to a steady body force $g_y = ng_o$. The ratio n denotes a factor by which the standard acceleration of gravity g_o on Earth (n = 1) can be reduced as on the ISS (n = 1×10^{-6}). Since the density field is coupled to the

This manuscript was accepted by Phys. Fluids. Click here to see the version of record.

body force, for ground-based laboratory conditions impending motion of the two fluids occurs without any stability threshold. Under an ideal initial condition the interface would be stationary, the two fluids can potentially be brought into intimate contact at the interface, x = L/2, and motion of the flow field would follow without any initial disturbance superimposed on the interface motion. For two fluids with similar thermophysical properties as in Table I of Appendix A, since the ideal initial condition cannot be obtained in a ground-based laboratory condition, it is necessary to separate the two fluids initially by a divider. Initial contact of the two fluids is established by removing the divider with a prescribed impulsive velocity $U_o(\delta(t))$. The removal of the divider introduces an impulsive disturbance on the interface for a short time duration τ, smaller than the time scale T_b of the bulk fluid $\tau << T_b$ to drive interface motion. The impulsive velocity perturbation may be approximated by a pulse function as

$$\vec{V}(L/2, y, z, t) = U_o[\delta(t) - \delta(t-\tau)] \tag{1}$$

where $\delta(t)$ and $\delta(t-\tau)$ represent a step function at time t = 0 and t = τ, in which $\tau = H/U_o$ is the pulse duration that depends on the prescribed pulling velocity U_o. The ideal initial condition at t = 0, $\vec{V}(L/2, y, z, 0) = 0$ corresponds to $U_o = 0$ which is defined as the sudden removal of the divider without any initial disturbance. Such an ideal condition is highly desirable since it implies, as predicted by the computational model[6], that symmetry would be obtained in the system for motion of the interface due to buoyancy-driven flow. The quest to find symmetry in the system is the challenge posed to experimentalists in the design of the experiment. As will be shown there is a range of critical impulsive velocity $U_o(\delta(t))$ for which symmetry can be approached; this is dependent on the balance between the injected kinetic energy due to divider motion and the driving initial potential energy of the system which is shown in Appendix B.

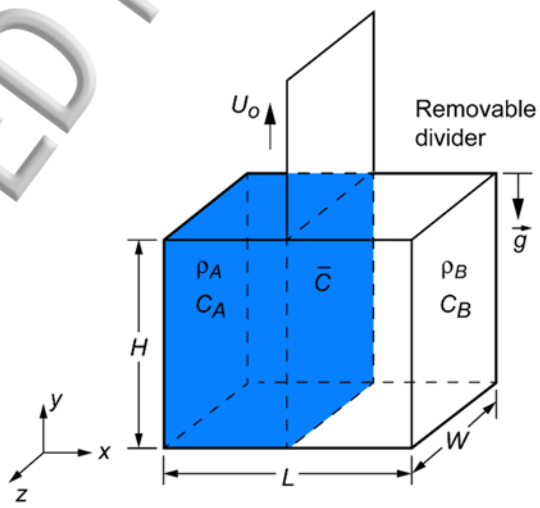

FIG. 2. Physical model and initial configuration of two liquids at an interface.

This manuscript was accepted by Phys. Fluids. Click here to see the version of record.

A. Description of mixing: ground-based conditions

For buoyancy-driven mixing under ground-based laboratory conditions, with ideal initial condition of no disturbance $U_o = 0$ as shown in Fig. 2, the interface motion is described by the advection-diffusion equation

$$\frac{\partial C}{\partial t} + (\vec{V}.\nabla)C = D_{AB}\nabla^2 C \tag{2}$$

subjected to the initial condition

$$C(x,y,z,0) = \begin{cases} C_A & 0 \le x < L/2 \\ \overline{C} & x = L/2 \\ C_B & L/2 < x \le L \end{cases} \tag{3}$$

This equation describes the motion of an initial material line $\overline{C}$ at the interface for two-dimensional motion or a flat surface in three dimensions. For the heavy fluid on the left the normalized concentration is $C_A = 1$, whereas for the light fluid on the right $C_B = 0$, and the interface has the prescribed average value $\overline{C} = 0.5$. The length stretch $\mathcal{L}(t)$ of the interface is determined from the Lagrangian history of $\overline{C}$ as shown in Appendix A. The characteristics of the flow field determine whether or not Eq. (2) is linear or nonlinear, the flow field

$$\vec{V} = \vec{V}(x,y,z,t;\Lambda) \tag{4}$$

as a function of its parametric space Λ can either be measured using particle image velocimetry or computed using the approximate mean field Boussinesq equations,

$$-\rho\frac{\partial \vec{V}}{\partial t} + (\vec{V}.\nabla)\vec{V} = -\nabla p + \overline{\mu}\nabla^2\vec{V} + \rho\vec{g} \tag{5}$$

Equations (5) express the description of the dynamical motion of the flow field, relative to its measurement using PIV in Part 2 and the flow field prediction of the approximate computational model[6]. The density field in Eq. (5), taken independent of pressure, is coupled to the concentration field via

$$\rho = \overline{\rho}(1 + \beta\Delta C) \tag{6}$$

in which, $\beta = 1/\overline{\rho}\,(\partial\rho/\partial C)$. Since there is no change of volume during ideal mixing, the condition of incompressibility is satisfied,

$$\nabla \cdot \vec{V} = 0 \tag{7}$$

This manuscript was accepted by Phys. Fluids. Click here to see the version of record.

However, there exists a limit in which the condition of incompressibility for two liquids may not apply under certain microgravity condition as pointed out in Ref. 48; this limit is given by the inequality $|\vec{g}|L_c < \nu D_{AB}$ in which L_c is the characteristic length of the enclosure, and ν the kinematic viscosity. For our experiments, this implies that for $|\vec{g}| < 10^{-10}$ the condition of incompressibility does not apply, however for the microgravity experiment[45] $|\vec{g}| O(10^{-2})$ satisfied the criterion for incompressibility.

The parametric space for the ideal initial condition[6] of stationary interface, that is no initial disturbance at the interface with $U_o = 0$, is obtained from dimensional analysis using Eqs. (2,5,7). Scaling of Eqs. (2,5,7) using the boundary condition of impermeability of the concentration field

$$\nabla C \cdot \vec{n} = 0 \tag{8}$$

along the boundary Γ_b of the cavity with normal $\vec{n}$ to the wall which also satisfies the no-slip condition

$$\vec{V} = 0 \tag{9}$$

along the wall of the cavity shows that the parametric space Λ_i for the ideal problem is a function of three parameters

$$\Lambda_i = \Lambda_i(Gr, Ar, Sc) \tag{10}$$

However for the non-ideal situation that we are considering, in which the initial impulsive velocity approximated by Eq. (1) injects a disturbance at the interface, introduces a pseudo-parameter in the problem characterized as the impulsive Reynolds number Re_i. Thus the enlarged parametric space becomes

$$\Lambda = \Lambda(Gr, \mathrm{Re}_i, Ar, Sc) \tag{11}$$

in which the Grashof number Gr, impulsive Reynolds number Re_i, aspect ratio Ar and Schmidt number Sc are given as

$$Gr = \frac{\Delta\rho}{\bar{\rho}} \frac{n g_o H^3}{\bar{\nu}^2}, \quad \mathrm{Re}_i = \frac{U_o H}{\bar{\nu}}, \quad Ar = \frac{W}{H}, \quad Sc = \frac{\bar{\nu}}{D_{AB}} \tag{12a, 12b, 12c, 12d}$$

Alternatively, the Peclet number Pe can be used which is defined as the product of Grashof and Schmidt number $Pe = Gr\,Sc$. However, if the scaling exponents of Gr and Sc are the same then, a reduced parametric space can be given as

$$\Lambda = \Lambda(Pe, \mathrm{Re}_i, Ar) \tag{13}$$

This manuscript was accepted by Phys. Fluids. Click here to see the version of record.

which is also tested using experimental data. The Peclet number *Pe* represents the ratio of mass transport by convection driven by the buoyancy force to that of molecular diffusion. The Grashof number *Gr*, the ratio of buoyancy to viscous force, represents the intensity of the flow field. The impulsive Reynolds number Re_i is a measure of the injected inertial force relative to viscous force in the system. This measure occurs over a short time scale τ relative to the advection time scale T_b of the interface caused by the flow field in response to the initial potential energy of the system; in the above equations, the overbars denote average values. The variation of width of the enclosure *W* as defined by the aspect ratio allows experimental simulation from an approximate two-dimensional (2D) Hele-Shaw cell to a full three-dimensional (3D) cavity. In relation to a 2D model, the variation of the *z*-plane aspect ratio $Ar = W/H$ is used, as shown in Fig. 2 to determine the range of aspect ratios for which the 2D approximation applies. In the variation of our parametric space, the ratio of diffusion of momentum to that of mass given by the Schmidt number in Eq. (12d), in which D_{AB} is the binary diffusion coefficient, is taken into account through thermophysical property variation as shown in Table I of Appendix A.

B. Metrics to characterize mixing

1. Length and time scales

Buoyancy-driven mixing is characterized using various descriptors which includes, length stretch $\mathcal{L}(t)$, interface width of the mixed region $\delta_w(t)$, and the mixing efficiency η_E. In the case of mixing by RT instability[31], a similar mixing width of the interface is used to characterize the dynamics of the system based on the penetration depth of the denser fluid. In our system, there is symmetry in terms of penetration depth of the light and dense fluid, so we define $\delta_w(t)$ as the average distance between concentration levels of 0.1 and 0.9. Though our problem has similarity to RT instability, it differs in certain basic factors such as, the initial condition, the stretching and folding prior to the birth of RTM, and the late stages. Even though the mixing width $\delta_w(t)$ is used as a measure to characterize our system, in the early stages its measurement is coarse due to averaging, the length stretch $\mathcal{L}(t)$ serves as a preferred metric for the buoyancy time scale T_b . In the late stages in which the two fluids become stably stratified, $\delta_w(t)$ is used advantageously as a metric to denote the extent of mass transport and hence can also be used as a global measure of the mixing efficiency of the system. We basically have two independent measurements, the length stretch $\mathcal{L}(t)$ to characterize the local kinematics and the mixing width $\delta_w(t)$ which is related to the mixing efficiency to characterize the quasi-equilibrium dynamic state of the system. We use the dimensionless length stretch, for short time events, as a metric defined as

$$\mathcal{L}(t) \equiv \frac{l(t) - l_o}{l_o} \tag{14}$$

where $l(t)$ is a measure of the elongation of the interface as a function of time and l_o is the initial length of the interface at time zero. Whereas the dimensionless mixing width $\delta_w^*(t)$ is defined as

$$\delta_w^*(t) \equiv \frac{\delta_w(t) - \delta_{wo}}{\delta_{wm}} \tag{15}$$

which represents the ratio of the mixed width $\delta_w(t)$ of the interface, with reference to its initial value δ_{wo}, and to the width representing a homogeneous mixed region δ_{wm}. δ_{wo} is the diffusive width of the interface at time t = 0 that depends on the resolution of the interface width initially and δ_{wm} is the resulting diffusive width as $t \to \infty$ which is equal to the height of the cavity in the limit.

The transient mixing characteristic of the two liquids is a problem with multiple time and length scales. In particular three time scales occur, a buoyancy time scale T_b, viscous diffusion time scale T_v, and mass diffusion scale T_D,

$$T_b = \frac{1}{\sqrt{\frac{ng_o}{H}At}}, \quad T_v = \frac{H^2}{\bar{\nu}}, \quad T_D = \frac{H^2}{D_{AB}}, \tag{16a, 16b, 16c}$$

where At is the Atwood number $At = \Delta\rho / 2\bar{\rho}$. The particular time scale of interest depends on the event[6] occurring during the mixing process. The characteristic length scale L_c is based on either the large length scale of the geometry (H, L, W) and interface width $\delta_w(t)$, or the small length scales based on the diffusion of mass and momentum or the striation thickness $S(t)$ of the interface defined in Part 2. The small length scale, based on the diffusion of mass and momentum, may be obtained from the short time solution of Eq. (2) for a semi-infinite domain $x \geq L/2$ when the nonlinear advective terms are negligible which is given by,

$$C(x,t) = \bar{C}\, erfc \frac{(x - L/2)}{2\sqrt{D_{AB}t}} \tag{17}$$

in which $L_c = 4\sqrt{D_{AB}t}$ due to symmetry; in analogy the length scale based on the diffusion of momentum is given as $L_c = 4\sqrt{\bar{\nu}t}$. Alternatively, the long time exact solution of Eq. (2) for negligible advective terms with boundary condition Eq. (8) can be shown to reduce to the one-dimensional solution given by,

$$C(x,t) = \frac{1}{2} + \frac{2}{\pi}\sum_{l=0}^{\infty} \frac{(-1)^l}{(2l+1)} \cos(2l+1)\pi\frac{x}{L} \exp -(2l+1)^2\pi^2(D_{AB}/L^2)t \tag{18}$$

In this form, the dependence on the mass diffusion time scale becomes apparent. Equations (17,18) apply to microgravity condition, in particular they show that the one-dimensional solution of the diffusion equation becomes independent of tilt-angle θ shown in Fig. 1; in this limit the Rayleigh-Taylor problem and the buoyancy-driven mixing problem become identical. This observation implies that microgravity condition $(ng_o = 10^{-6} g_o)$ can stabilize the unstable RT arrangement in ground-based condition $(ng_o = 1g_o)$; this is in contrast to stabilization of RT due to surface or interfacial tension that occurs in ground-based laboratory condition. This can be understood based on linear stability theory in Ref. 49, of two viscous superposed equi-viscosity fluids, which indicates that the maximum growth rate

This manuscript was accepted by Phys. Fluids. Click here to see the version of record.

$$n_m \approx (\pi n g_o A t / \lambda_m)^{1/2} \tag{19}$$

corresponding to the most unstable wavelength

$$\lambda_m \approx 4\pi(\bar{v}^2 / n g_o A t)^{1/3} \tag{20}$$

approaches zero under microgravity condition; this is because the most unstable wavelength becomes much greater than the cavity size $\lambda_m >> L$, the unstable RT arrangement in ground-based condition $(ng_o = 1g_o)$ becomes stabilized in microgravity condition $(ng_o = 10^{-6} g_o)$.

2. Experimental mixing efficiency

For our experimental configuration, the mixing efficiency can be determined from the ratio of how much of the initial potential energy is used to mix the two liquids in relation to the energy dissipated by viscosity estimated in Part 2. However, we use a measure of the mixing efficiency based on the kinematical model[18] for internal wavebreaking event which is defined as the ratio of potential energy gained from the system through the creation of a stratified mixed layer to the total energy input from the potential energy released as the system overturns. We show that the mixing efficiency determined from energy exchange is related to the kinematic measurement of the interface and provides a convenient measure of mixing efficiency. In order to quantify the effectiveness of mixing driven by the initial potential energy of the system, we define the experimental mixing efficiency,

$$\eta_E = \frac{\Delta PE - \Delta PE_{\min}}{\Delta PE_{\max} - \Delta PE_{\min}} \tag{21}$$

similar to Ref. 32 in terms of the change of potential energy between observed initial and final state weighted in terms of the (maximum) / (minimum) change in potential energy which yields (uniform mixing) / (no mixing); this definition is analogous to that used in Ref. 18. The change in potential energy of the system from the initial configuration of unstable stratification to an observed final state is given as

$$\Delta PE = \int_0^W \int_0^L \int_0^H gy(\rho(y) - \rho_B) dy dx dz \tag{22}$$

This change in potential energy gives rise to a transfer of momentum which involves a loss of kinetic energy and the resulting mixed fluid layer represents an irreversible gain in potential energy; while the denominator in Eq. (21) represents the maximum potential energy released. For the case in which there is no mixing, the heavy fluid settles to the bottom and the light fluid on top, an energy balance between the two configurations in which the two fluids simply exchange position shows that this gives rise to the minimum change in potential energy which is given by

This manuscript was accepted by Phys. Fluids. Click here to see the version of record.

$$\Delta PE_{\min} = \frac{1}{8}\Delta\rho n g_o \forall H \tag{23}$$

A similar energy balance in which the final configuration results in homogeneous mixing of the two fluids with a uniform background based on the light fluid shows that a maximum change of potential energy occurs given as

$$\Delta PE_{\max} = \frac{1}{4}\Delta\rho n g_o \forall H \tag{24}$$

The potential energy change can be scaled with the initial potential energy $PE_o = 1/2\Delta\rho n g_o \forall H$ to define the potential head or dimensionless mixing height as $y^* = \Delta PE / PE_o$, where $\forall = WHL$ is the volume. This definition allows the mixing efficiency of Eq. (21) to be defined in terms of kinematic measurement of the height of the resulting stratification layer; when the dimensionless mixing height is re-scaled as $y^* = y/4h_o$, the mixing efficiency takes the simple form of

$$\eta_E = \frac{y - h_o}{h_o} \tag{25}$$

In the above equation $y(t) \geq h_o$ is the total height of the resulting mixed stratified layer measured relative to the bottom of the cavity, and $h_o = H/2$ corresponds to the quasi-equilibrium height for the case of no mixing. This definition differs from the case of RT instability, for it allows the efficiency to vary from zero to one, whereas RT varies from zero to one-half[32]. The height of the mixed stratified layer $y(t)$ is related to the mixing width $\delta_w(t)$ and defined relative to h_o as

$$y(t) = h_o + \delta_w(t)/2 \tag{26}$$

The width of the interface $\delta_w(t)$ is measured relative to the stably stratified configuration for the case of no mixing; this definition takes into account that the heavy and light fluids penetrate the top and bottom layer symmetrically in the stably stratified configuration when mixing occurs, and $\delta_w(t) \to 2h_o$ as $t \to \infty$.. The expression for $y(t)$ in Eq. (26) allows a convenient measure of the final configuration of the interface after the transient dynamics decay. η_E is a global measure of potential energy conversion by the flow field to drive mixing which characterizes the approach to a quasi-equilibrium state of a stably stratified configuration, whereas $\mathcal{L}(t)$ characterizes the non-equilibrium local dynamics. An alternative method to determine the mixing efficiency based on $\mathcal{L}(t)$ is detailed in Part 2 that employs the mechanical mixing model based on continuum mechanics and shows in Fig. 9 (c) comparable results to Eq. (25).) (A similar definition of mixing efficiency has been used in Ref. 18 for multiple wavebreaking events inside a tank and yields comparable results to experiments in Ref. 19, the main assumption used in the model is that wavebreaking events are localized in small volumes relative to the tank and external source of kinetic energy can be neglected for these events, hence the conversion of kinetic energy of the flow is directly transferred into gravitational potential energy; the same assumption applies to the single wavebreaking event in our experiments and our experimental mixing efficiencies are comparable to reported values in Refs. 18,19).

IV. EXPERIMENTAL RESULTS

We discuss experimental results obtained using the full-field view (FFV) method in comparison to the planar laser-induced fluorescence (PLIF) method for fixed Schmidt number Sc = 3333.

A. Global view of interface: Full-field view (FFV) method

The essence of buoyancy-driven mixing, stretching and folding of the interface between two liquids from its initial time zero to its final stably stratified configuration driven by the flow field is shown in Fig. 3(a). In contrast to mechanical equilibrium, under microgravity condition on ISS with a body force of O ($10^{-6} g_o$), which would stabilize the initial configuration of the interface at time $t = 0$, ground-based condition with a body force of O ($1g_o$) drives buoyancy-induced flow field caused by hydrostatic pressure imbalance due to the body force according to Eq. (5). The intensity of the flow field given by Eq. (5), gives rise to the nonlinearity of the advective terms in the advection–diffusion given by Eq. (2), that causes stretching and folding of the interface. Buoyancy-driven mixing is shown for the parameter $Gr = 3.18\times10^6$ or $Pe = 1.06\times10^{10}$ given in Table I of Appendix A, with impulsive Reynolds numbers of Re_i = 1500, 2500, and 3500 and corresponding divider impulsive velocities of $U_o = 3, 5, 7$ (cm/s) for a cavity with width $W=1cm$.

Insight on the effect of the impulsive velocity of the divider motion on interface configuration may be obtained from Eq. (B5) of Appendix B, which states that the total initial energy E_{To} consists of injected kinetic energy KE of divider motion and initial potential energy PE_o. The impulsive velocity, characterized by impulsive Reynolds numbers of Re_i, affects the injected kinetic energy KE that determines the approach to symmetry of the interface structure while the potential energy PE_o drives folding. The characteristic values for the initial potential energy PE_o , injected kinetic energy KE, and flow field velocity magnitude U_C from energy balance model are shown as a function of impulsive Reynolds number Re_i in Table II of Appendix B.

In relation to interface configurations at $t = 2\ s$ in Fig. 3(a), the relative magnitudes of the initial potential PE_o to injected kinetic energy KE serve as descriptor of interface perturbation or disturbance. According to Table II of Appendix B, the global injected kinetic energy based on linear KE_L and uniform KE_U velocity profiles for the entire cavity bound the local impulsive kinetic energy based on linear KE_{iL} and uniform KE_{iU} velocity profiles at the interface region limited by the boundary layer thickness due to divider motion; the local velocity profile approximations accounting for the boundary layer thickness owing to divider motion result in local minimum and maximum values of KE_{iL} and KE_{iU} respectively. The various approximations show a range of possible injected kinetic energies, however the local maximum value of the impulsive kinetic energy KE_{iU} based on uniform velocity in the boundary layer is used as a basis to compare to the initial potential energy PE_o to assess perturbation effects on the interface, and shows in Fig. 3a that interface disturbance increases with the increase of injected kinetic energy or impulsive Reynolds number Re_i for t = 2 s. For the range of impulsive Reynolds numbers with $1500 \le \mathrm{Re}_i \le 3500$, the ratio of initial potential energy to impulsive kinetic energy corresponds to the range of

This manuscript was accepted by Phys. Fluids. Click here to see the version of record.

$3.36 \le PE_o / KE_{iU} \le 11.94$ which shows that as the injected kinetic energy increases symmetry is approached, and interface disturbance also increases with minimum $PE_o / KE_{iU} = 3.36$ corresponding to $Re_i = 3500$.

For $Re_i = 1500$, the initial potential energy PE_o is greater than the injected kinetic energy KE_{iU}; thus as shown *for* $t = 2\ s$, the stretching of the interface is relatively smooth though asymmetric as the bottom fluid penetrates farther than the top. In contrast, keeping the potential energy constant and increasing the impulsive Reynolds number to $Re_i = 3500$ at $t = 2\ s$ shows a perturbed interface with the increase of KE_{iU}. At the early stages of $t = 2\ s$, density current at the bottom of the cavity causes frontogenesis due to the sharp density front; this is similar to phenomenon that occurs in lock-exchange flows [40,41].

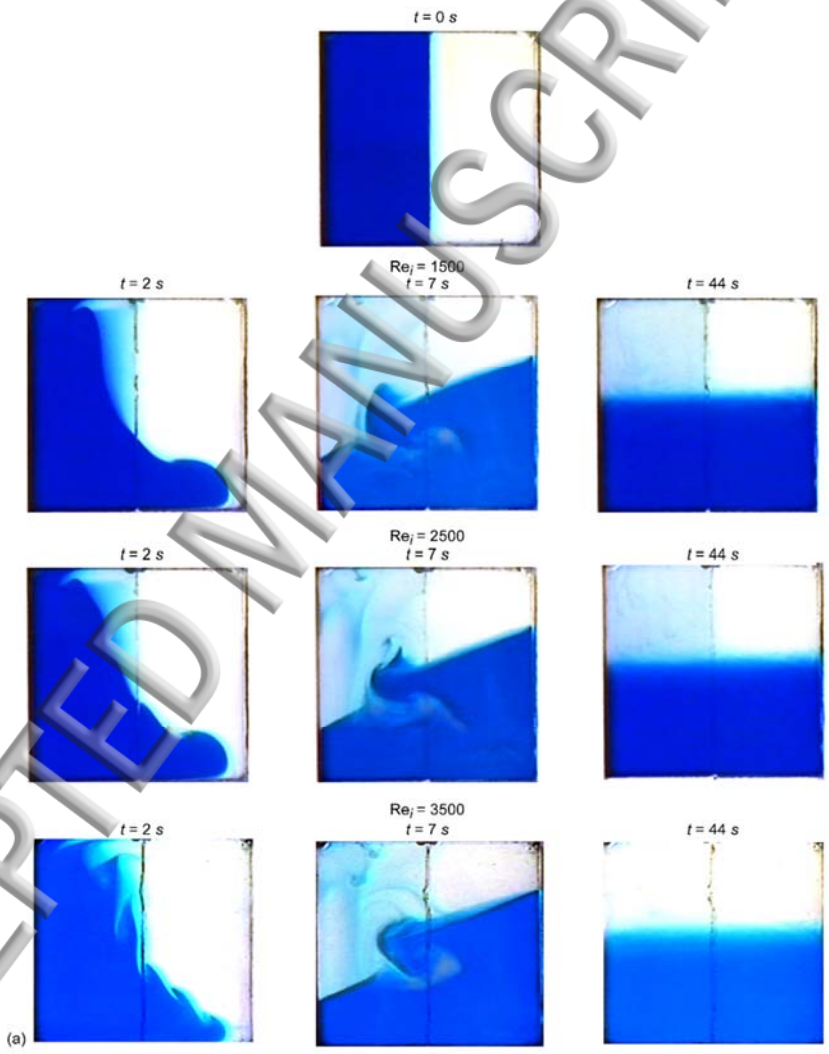

FIG. 3. Evolution of the interface as a function of time showing the effect of impulsive Reynolds number Re_i constrasting the full-field view (FFV) method and planar-laser induced fluorescence (PLIF) method. (a) Stretching and folding of interface during mixing by buoyancy-driven flow, that produce the Rayleigh–Taylor morphology (RTM) structure at t = 7 s for Gr = 3.18×10^6 or Pe = 1.06×10^{10}, Ar = 0.2, FFV method.

The configurations of the interface at $t = 7\ s$, stemmed from the overturning motion that produced the ideal condition for the growth of a single wavelength RT instability, that unfolds to

This manuscript was accepted by Phys. Fluids. Click here to see the version of record.

a spanwise RT morphology (RTM) structure which consists of a spike or left penetrating front and bubble or right penetrating front, analogous to the results in Ref. 50. The two-dimensional computational model[6] shows RTM occurs for a range of Grashof numbers and its orientation can shift from approximately 30^0 with respect to a horizontal axis as shown for $t = 7\ s$ at mid-height of the cavity, to a 90^o orientation as the Grashof number increases. The 90^o orientation shown in the computational model[6] is analogous to the unstable stratified configuration of the RT instability when excited via a long wavelength initial perturbation as shown in Refs. 51-55.

In relation to the experiments, the computational model[6] which is based on the ideal initial condition, captures the large scale features of the interface morphology, though these features are predicted to be symmetric. The experiments based on non-ideal initial condition show that the delay caused by the divider motion gives rise to asymmetry. The lifetime of the short-lived coherent RTM structure at $t = 7\ s$, with the ubiquitous feature of the Rayleigh-Taylor morphology, in on the order of $2\ s$. The roll-up feature at $t = 7\ s$ near the top and bottom edge of the structure is evident; the image of the top structure is also shown by the lighter penetrating fluid below for $Re_i = 1500$. Finding two fluids with color contrast which would show a sharp image of the bottom structure poses an experimental challenge, as well as measurement of the length stretch of the interface; this is because of the enhanced local molecular diffusion that accompanies folding owing to the existence of a hyperbolic point in the flow field as will be shown in Part 2.

A solution to the symmetry problem is to increase the impulsive Reynolds number to $Re_i = 2500$, however, this causes the initiation of Kelvin-Helmholtz (KH) instability waves due to the intense shearing motion of the divider for t = 2 s. In comparison to $Re_i = 1500$, there is a transition between shear instability produced by the relative velocity between the heavy sinking fluid and lighter rising fluid, and that due to shear divider motion. The computational model[6] indicates that the effect of relative velocity between two fluids for short times can produce KH instability in absence of divider motion. The increase in impulsive Reynolds number to $Re_i = 2500$ causes further approach to symmetry at $t = 7\ s$, however the features of the short-lived coherent RTM structure tend to be diffused as Re_i increases; the contrasting events for $Re_i = 1500$ and 2500 capture the challenge posed toward the search for symmetry in the system.

The effect of intense shear motion due to the divider is to cause KH shear instability at the interface for short times when Re_i increases to 3500. This is illustrated for $t = 2\ s$ which shows a combination of KH waves near the bottom that transition to billow clouds[56] near the top of the cavity produced by the KH mechanism. The approach to symmetry at $t = 7\ s$ shows a modified morphology of the interface, since the roll-up features become more pronounced. The late stage of RTM for $t > 7\ s$ shows the characteristic feature of an internal breakwave[57]. As time increases, a catastrophic global bifurcation[6] occurs, the RTM structure collides with the wall which is shown below in the Multimedia view for $Re_i = 3500$ using the PLIF method in section B; this event annihilates the RTM structure and causes enhanced local molecular diffusion. Self-induced sloshing of the interface follows, which decays nearly periodically toward stable stratification; the net effect of advection and molecular diffusion is indicated by the diffusive region at the interface at the settling time $T_f = 44\ s$ for stratification.

The basic features of stretching and folding and the dynamics toward stratification have been captured in the computational model[6]. However in the computational model, symmetry is

predicted because the ideal model problem is considered; that is the interface evolves from its initial configuration without any initial impulsive disturbance due to motion of the divider $U_o = 0$. In the final state, the two fluids then becomes homogeneous or mixed over a much longer time scale denoted by T_D, the molecular mass diffusion scale. In between the two limits of mixing, segregation at time zero and approach toward homogenization after stratification, the emergence of complex patterns occurred for increasing Grashof or Peclet numbers. In terms of the basic mixing structures, whorls and tendrils, as originally defined in Ref. 58, the RTM structure is described as whorl-like; examples of whorls and tendrils in relation to buoyancy-driven mixing occur when the body force field is oscillatory [26-28] or stochastic[30] and also for steady body force at high Grashof[6] or Peclet numbers.

1. Interaction of pressure gradient and density gradient

The effect of the pressure gradient can be considered by examining its relation to the density gradient shown for the initial configuration shown in Fig. 3(a) (t=0), which shows that initially there is a hydrostatic pressure gradient ∇p that acts in the vertical direction relative to the density gradient $\nabla\rho$ in the horizontal direction. The coupling of these gradients $(\nabla\rho\times\nabla p)$ yield the baroclinic vorticity production term in the vorticity equation that causes flow for the case of low impulsive Reynolds numbers ($Re_i = 1500$ in Fig 3(a)) in which the interface is relatively unperturbed, and vorticity $\vec{\omega} = \nabla\times\vec{V}$ deposition on the interface for the case of high impulsive Reynolds numbers in which the interface is highly perturbed ($Re_i = 20{,}000$ in Fig 3(b).

The vorticity equation can be obtained from the curl of the Navier-Stokes Eq. (5) and yields $D\vec{\omega}/Dt = \vec{\omega}\cdot\nabla\vec{V} - \vec{\omega}\nabla\cdot\vec{V} + \bar{\nu}\nabla^2\vec{\omega} + (\nabla\rho\times\nabla p)/\rho^2$ which states that the rate of change of vorticity is due to vortex tube stretching and twisting in the first two terms followed by the diffusion of vorticity, and the baroclinic production of vorticity $(\nabla\rho\times\nabla p)$ due to interaction of density gradient and pressure gradient. For our two-dimensional cavity approximation the vortex tube stretching and twisting terms go to zero and the vorticity equation simplifies to $D\vec{\omega}/Dt = \bar{\nu}\nabla^2\vec{\omega} + (\nabla\rho\times\nabla p)/\rho^2$. In relation to Fig. 3(a) of our experimental configuration, the production of vorticity $(\nabla\rho\times\nabla p > 0)$ ensues for $t > 0$ caused by vorticity generated by the interaction of the vertical hydrostatic pressure gradient ∇p and the perpendicular density gradient $\nabla\rho$ which creates a torque that results in overturning motion of the two fluids which becomes stably stratified $(t = 44\,s)$ through the decay of vorticity from viscous diffusion. Note that the interface is relatively unperturbed for the low impulsive Reynolds number scenario of $Re_i = 1500$. In the stably stratified configuration $(t = 44\,s)$, the density gradient is parallel to the pressure gradient thus the baroclinic vorticity $(\nabla\rho\times\nabla p = 0)$ goes to zero.

2. Limit of high impulsive Reynolds number

The results for low impulsive Reynolds numbers show that since the divider cannot be removed instantaneously there is a delay in terms of fluid penetration between top and bottom which causes asymmetry. The limit of instantaneous removal of the divider to approach symmetry via increasing the impulsive Reynolds number by a factor of six to $Re_i = 20{,}000$ in Fig. 3(b), shows that impulsive motion of the thin polyethylene divider of width 0.1 mm produces a wake instability initially, due

ing shedding of the viscous boundary layer on the face of the divider which generates a vortex sheet component that is coupled to buoyancy instability due to interaction of density gradient $\nabla\rho$ and pressure gradient ∇p across the interface. The coupling of the vortex sheet component and buoyancy instability give rise to mixed mode KH and impulsive RT instabilities at the interface for the short time scale. (The impulsive RT instability is generated by the impulsive velocity perturbation at the interface given by Eq. 1, analogous to the impulsive RT generated by an impulsive acceleration field given in Ref. 50 by $\mathbf{g} = \Delta\vec{V}\delta(t)$ where $\Delta\vec{V}$ is the velocity change imparted by the impulsive acceleration and $\delta(t)$ is the Dirac delta function. In this limit there is a combination of KH instability waves near the top of the cavity at $t = 0.18$ *s* and impulsive RT instability near the bottom.

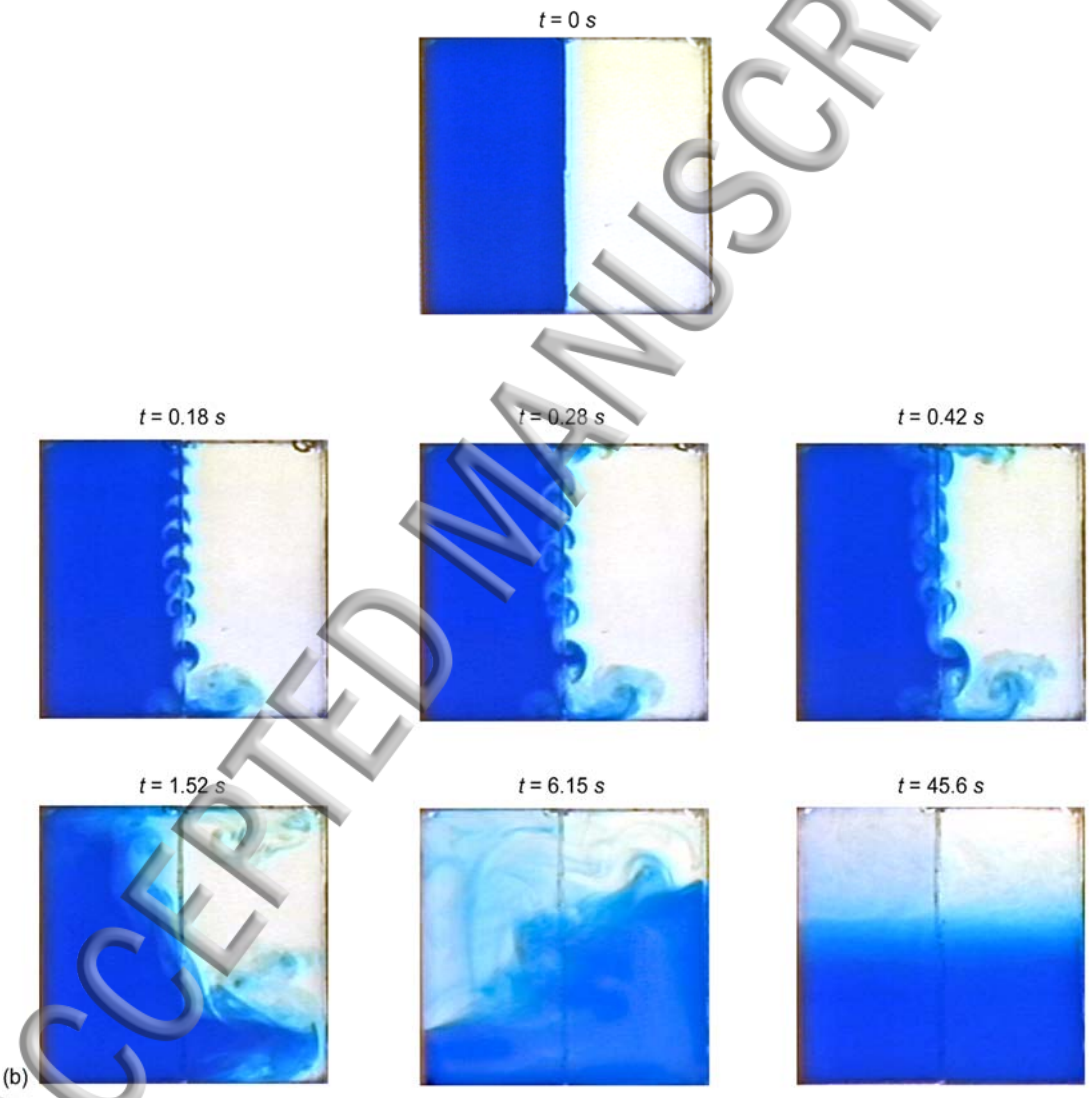

FIG. 3. –Continued. (b) Evolution of mixed mode instabilities,Kelvin-Helmholtz and impulsive Rayleigh-Taylor that generate the Richtmyer-Meshkov instability, at the interface over a short time scale $0 < t \leq 0.42$ s due to large impulsive Reynolds number $Re_i = 2.0\times10^4$ and transition to folding ($t > 1.52$ s) of a diffused interface for $Gr = 3.18\times10^6$ or $Pe = 1.06\times10^{10}$, $Ar = 0.2$, FFV method

The impulsive RT instability at the bottom-half of the cavity is due to the larger jump in pressure gradient which excites the short wavelength modes whereas the fluid near the top of the cavity is subjected to a decrease in pressure gradient, thus the relative shear motion of the divider and the two fluids become dominant and cause KH waves for short times $t \le 0.18\ s$. These structures are similar to the classical shear instability KH waves[56] simulated inside tanks. However for $t > 0.18\ s$ the instability amplifies through the interaction of the vertical pressure gradient across the perturbed interface with the horizontal density gradient which creates baroclinic vorticity $(\nabla\rho\times\nabla \mathrm{p})$ oriented out of page shown at t = 0.28 s and generates an incompressible Richtmyer-Meshkov instability at the interface typified by the mushroom structures.

For short times $0.18\ s < t \le 0.42\ s$, the growth of the interfacial instability is dominated by the impulsive RT instability mechanism which is analogous to shock-driven RT instability known as the Richtmyer-Meshkov instability[50], as exemplified above for the impulsive velocity-driven RT instability; coarsening of the interface over the short time scale results in a nearly diffused interface at t = 0.42s. According to linear theory of stability given by Eq. (20), the most unstable wavelength $\lambda_m \approx 0.54cm$ fall within the range of the measured structures which is approximately $\lambda_{\exp} \approx 0.625cm$; the inverse growth rate Eq. (19) of the instability is predicted to be $n_m^{-1} \approx 0.37\,\mathrm{s}$ which is in the range of the short time scale interval. The KH and impulsive RT instabilities generated initially serve as a source to drive molecular diffusion at the interface which produce a diffused interface. The stretching of the diffused interface at $t = 1.52\ s$ is in contrast to the sharp interface for lower impulsive Reynolds number in Fig. 3(a); this is because of the small ratio of driving potential energy to injected impulsive kinetic energy $PE_o / KE_{iU} = 0.25$, indicating that the injected impulsive kinetic energy becomes greater than the driving potential energy. The resulting overturning motion produces folding of the diffused interface at $t = 6.15\ s$ which does not show the features of RTM shown in Fig. 3(a) as symmetry is approached. This indicates that if the injected kinetic energy is much greater than the initial potential energy, then the interface becomes diffused and the feature of RTM does not exist. This finding underscores the delicate balance between the injected kinetic energy into the system to approach symmetric folding and the propensity of the interface structure of the interface to become diffused.

3. Relationship between shock-induced RM instability and impulsive velocity-induced RM instability

Analogy between the Richtmyer-Meshkov (RM) instability, for shock-induced compressible gas in a shock-tube through linear stability analysis (Ref. 59), and impulsive velocity-induced experiments using incompressible nonhomogeneous liquids in a cavity with low and high impulsive Reynolds numbers shown in Fig. 3(a) and Fig. 3(b), is made to highlight the similarities and differences between the two systems. RM instability is the instability that occurs at a planar interface separating two gases that is impulsively accelerated by planar shock wave travelling in the direction of the normal to the interface. The difference between shock-induced RM and impulsive velocity-induced RM is that in the former pressure gradient accelerates a background shear flow normal to the interface whereas in the latter the pressure gradient accelerates a background rotational flow (see Part 2) in the same direction as the interface.

Consider two hypothetical situations in reference to Fig. 3 of two gases separated by an interface, in which an incident shock wave moves from the left boundary impinging on the planar interface (Fig. 3(a)), and an incident shock wave impinging on a quasi-sinusoidal interface (Fig. 3(b); in this hypothetical situation the pressure gradient would be normal to the interface or aligned in the same direction as the density gradient. The coupling of density gradient and pressure gradient amplifies perturbations at the

ing face through the mechanism of baroclinic vorticity generation resulting from the misalignment of the pressure gradient of the shock wave and the density gradient across the interface to generate the Richtmyer-Meshkov instability for shock-driven instability. In contrast, for our experiments, the hydrostatic pressure gradient of the two liquids in Fig. 3(a) and Fig. 3(b) is perpendicular to the density gradient across the interface and two types of scenarios occur, global and local. For the global scenario that occurs with the low impulsive Reynolds number in Fig. 3(a), the interface remains sharp and the baroclinic vorticity generation, generates an overturning motion that leads to stratification. Whereas, for the local scenario with high impulsive Reynolds number in Fig. 3(b), the impulsive velocity-induced perturbation generates kinks at the interface initially (similar to Fig. 3(a) for Re_i = 3500 (t = 2 s) however oriented vertically with an increase in mode numbers) through KH instability mechanism that amplifies the interface perturbation through baroclinic vorticity generation. Since the kinks form a quasi-sinusoidal interface, the vorticity distribution from coupling of the pressure gradient and density gradient along the interface results in increasing amplitude of the sinusoidal-perturbed interface and generates the mushroom structures (t = 0.28 s) that represent the signature of the Richtmyer-Meshkov instability.

A quasi-sinusoidal perturbed interface has also been generated in shock-tube experiments (Refs. 60) from pulling a thin flat plate horizontally that separates the gases, however, a diffuse interface is created by this method. Though, the late stages of the instability between shocked-induced compressible flow and our impulsive velocity-induced incompressible flow model differ, but they share the commonality of the mushroom interface region becoming locally homogeneous. In the late stages, the shocked-induced interaction with the interface transmits a shock wave and reflects a shock wave or a rarefaction wave from the interface, and reshock occurs because of reflection from the endwall of the shock tube (Ref. 59); whereas, in our experiments a global overturning motion occurs from global baroclinic vorticity generation that overturns the entire perturbed interface.

The scenario between the relatively unperturbed interface for low impulsive Reynolds number and perturbed interface for high impulsive Reynolds number is also analogous to linear stability analysis (Ref. 59) that considers the collision of a plane shock with a flat interface discontinuity and the resulting instability when the shape of the initial interface discontinuity is perturbed. The initial value problem with a jump discontinuity constitutes a Riemann problem and the one-dimensional solution of the Riemann problem for a shock-interface interaction serves as base solution for the small-amplitude, sinusoidally perturbed interface, of the linear theory of RM instability (Ref. 59). The results from linear theory were found to agree with an impulsive model when the incident shock is weak (Ref. 59). The impulsive model was developed by Richtmyer (Ref. 50) from the realization that compressible gas shock-driven instability could be modeled using incompressible nonhomogeneous liquids, in which the shock is induced through an impulsive body force. The analysis of the impulsive model is based on the Rayleigh-Taylor instability for constant acceleration, however the acceleration term is replaced by an impulsive body force acceleration (in which $g = \Delta u_0 \delta(t)$ is an instantaneous delta function $\delta(t)$ acceleration representing the shock and Δu_0 is the velocity jump across the interface imparted by the shock) coined as the impulsive Rayleigh-Taylor instability (Ref. 50); this is similar to the impulsive accelerating containers of incompressible fluids experiments in Ref. (50). A number of experiments have been designed with special arrangement to generate shock-induced through the body force, and have shown that indeed shock-driven by impulsive acceleration through the body force can generate RM instability using incompressible nonhomogeneous fluids (Ref. 50). In our model experimental problem, we show that the Richtmyer-Meshkov instability can be generated from impulsive-velocity perturbation initial condition in Fig. 3(b). Our experiments with the impulsive velocity initial condition between two fluids serve as analog to impulsive acceleration experimental model and the impulsive model of linear stability analysis, and show a novel method to generate short time Richtmyer-Meshkov instability for certain range of parameters shown in Fig. 3(b) for $0.18\ s < t \leq 0.42\ s$.

B. Local view of interface: Planar laser-induced fluorescence (PLIF)

In contrast to the FFV method which captures a global view of the interface, a local view of the mid-plane section of the cavity is shown in Fig. 3(c) using PLIF which captures the local details of the interface. The refractive index of the two dilute liquids are nearly matched such that light scattering is negligible, as evidence from the two nearly uniform regions separating the interface at t = 2 s. There exists local details not captured by the FFV method such as the effect of the injected vorticity due to divider motion produced by the wake, which is evident near the top of the interface for Re_i = 1500 and 2500 as well as resolution of kinks due to shear motion of the divider. Similar observation of vorticity injection was made in Ref. 34 for the design of a nearly frictionless barrier to initiate RT instability.

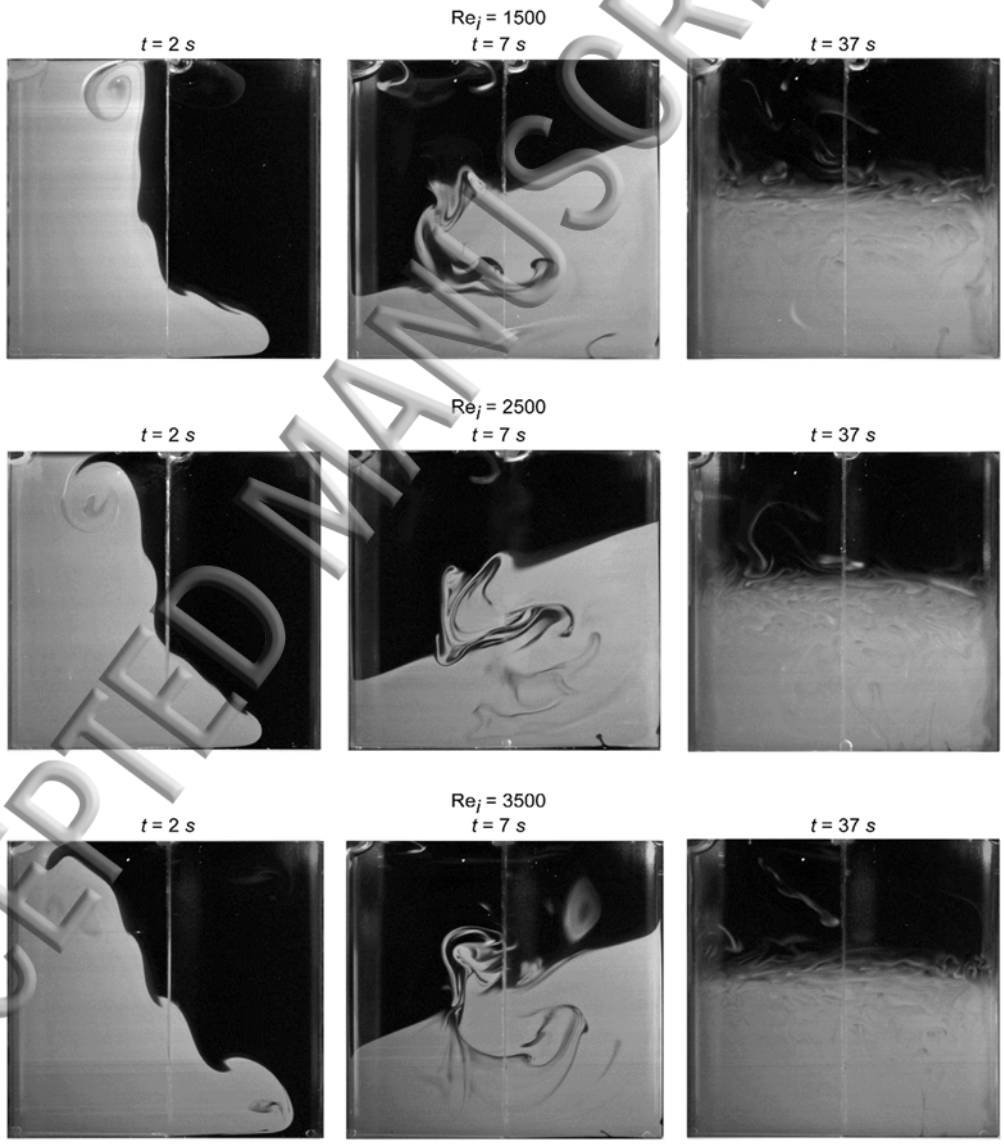

FIG 3. –Concluded. (c) Stretching and folding of interface, during mixing by buoyancy-driven flow, that produce the Rayleigh–Taylor morphology (RTM) structure at t = 7 s for Gr = 3.18×10^6 or Pe = 1.06×10^{10}, and Ar = 0.2, PLIF meth

The lower limit of impulsive Reynolds number $Re_i = 1500$, for which shear driven instability due to divider motion is minimal in comparison to the parallel shear flow due to buoyancy at the interface, shows the evolution of KH instability waves t = 2 s in Fig. 3(c). In comparison to the FFV method, the higher resolution of the PLIF method captures the local kinks at the upper section of the cavity and roll-ups behind the nose of the gravity current that shows frontogenesis near the bottom. The threshold of the impulsive Reynolds number determines the dominant mechanism, divider motion or buoyancy flow, for generating shear instability. For $Re_i = 1500$, the early stage of interface folding at $t = 7\ s$ shows two bubbles underneath the RTM front, the first bubble transitions to a roll-up behind the head of the RTM front and the second transitions to an elongated bubble with RTM morphology; see Multimedia view for $Re_i = 1500$.

The unfolding of the Rayleigh-Taylor morphology is seen most clearly for $Re_i = 2500$ at $t = 7\ s$ as well as the asymmetric penetration of the bubble in the pairwise RTM structure. When the effect of the injected kinetic energy increases such that the ratio of $PE_o / KE_{iU} = 3.36$ for $Re_i = 3500$ as shown in Table II of Appendix B, the intense shearing motion increases the effect of KH instability waves ($t = 2\ s$) at the interface which is shown near the bottom of the cavity whereas the top region shows kinks; the 3D global view of the FFV method in Fig. 3(a) indicated billow clouds[56] produced by the KH mechanism near the top region of the interface, which is projected as kinks on the 2D plane view of PLIF. Thus both the induced shear due to divider motion and intrinsic shear due to buoyancy-driven flow generate KH instability. However as the overturning motion occurs the shearing motion of the flow produces deep fingers at the location of the kinks (t = 2s) that grow and form local whorl structures that merge and self-organize into the RTM structure shown for $t = 7\ s$. The RTM front transitions to internal breakwave and its breakdown from wall and internal collision generates sloshing which decays toward stable stratification, see Multimedia view for $Re_i = 3500$; the large scale features of RTM are self-similar for the range of Re_i shown.

od; see Multimedia view for $Re_i = 1500$ and $Re_i = 3500$.

1. The birth of the RTM structure

Even though the birth of the RTM structure[6] is predicted to occur in the neighborhood of $Gr = 3\times10^5$ for 2D, careful experiments with $Gr = 3.7\times10^5$ or $Pe = 1.23\times10^9$ show the embryonic stage of RTM to be in existence during transition from aspect ratio of 0.2 to 0.3. As shown in Fig. 4 for $Re_i = 1000$ and $Ar = 0.2$, the initial potential energy PE_o is not sufficient to generate unstable density stratification so the interface displaces from its equilibrium configuration, mid-height of the cavity, to a right tilt at $t = 19\ s$; the restoring force of the interface causes the self-induced sloshing to decay, similar to an overdamped system, which leads to stable density stratification as shown for $t = 96\ s$. As the size of the cavity increases to $Ar = 0.3$, the initial potential energy reaches the critical value ($PE_{oc} = 1/2 V_c n g_o \Delta\rho H$, $V_c = W_c H L$) necessary to generate overturning motion that leads to unstable density stratification. The genesis or embryonic stage of the RTM structure is shown to occur at this value of the aspect ratio. The divider impulsive pulling velocity U_o is kept the same for $Ar = 0.2$ and $Ar = 0.3$ ($Re_i = 1000$); though, the initial potential energy and injected impulsive kinetic energy increase, their ratios $PE_o / KE_{iU} = 2.52$ remain equal for

This manuscript was accepted by Phys. Fluids. Click here to see the version of record.

$Ar = 0.2$ and $Ar = 0.3$ because of volume independence. At this threshold of Re_i or PE_o / KE_{iU}, the interface is smooth initially; the difference between the interface configurations for $Ar = 0.2, 0.3$ at $t = 5\ s$ stems from the increase in initial potential energy which increases the density current at the bottom of the cavity and leads to frontogenesis. These two cases contrast the relationship between the injected kinetic energy and the available initial potential energy to drive overturning motion, and show that there is a delicate balance between potential and injected kinetic energy for which the RTM structure exists.

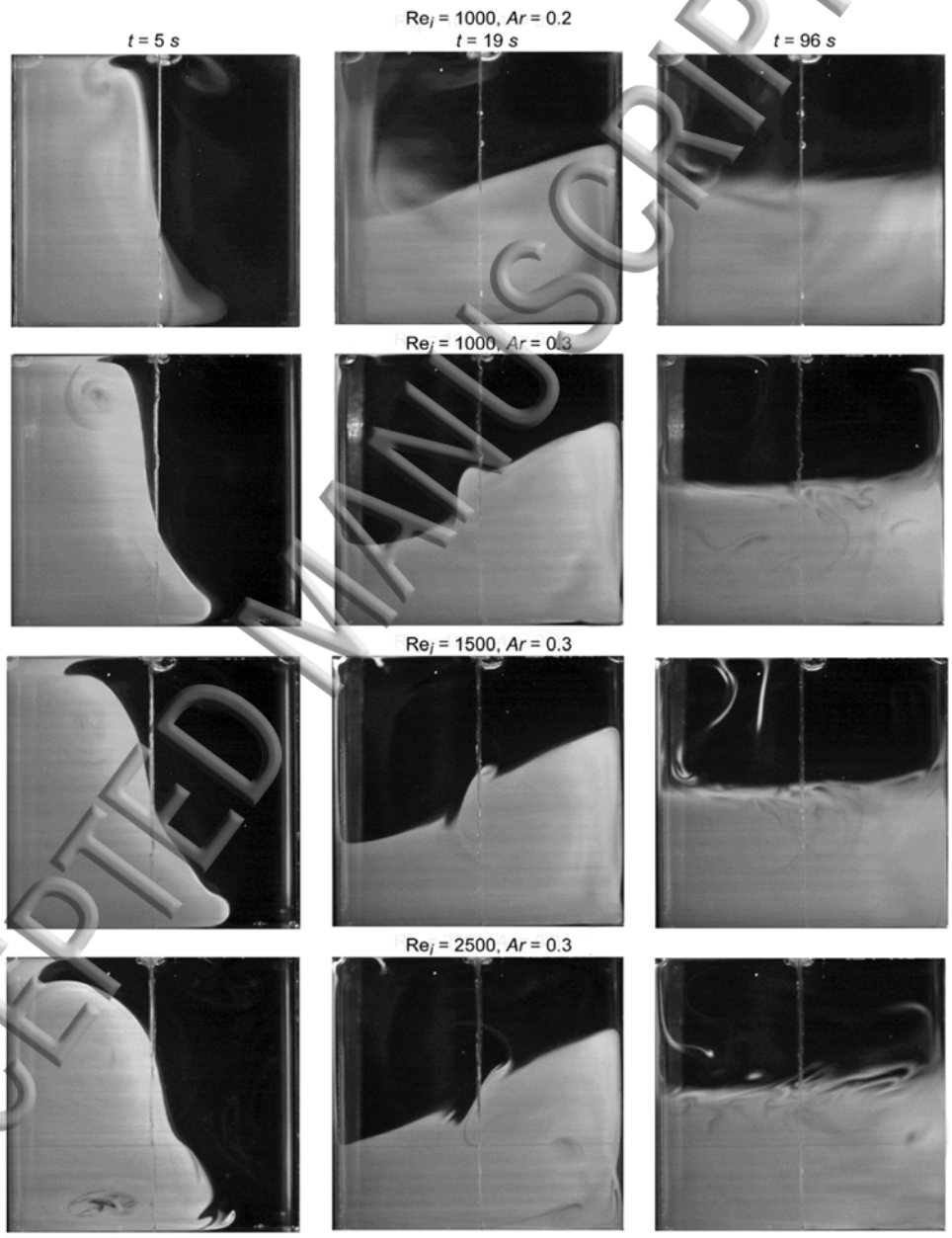

FIG. 4. Effect of aspect ratio Ar and impulsive Reynolds number Re_i on bifurcation of the interface showing transition from stretching (Ar = 0.2) to folding (Ar = 0.3) for $Re_i = 1000$ during genesis of the RTM structure for Gr = 3.7×10^5 or Pe = 1.23×10^9; and overshoot of the approach to symmetry between $Re_i = 1500$ and $Re_i = 2500$ for Ar = 0.3.

Subsequent increase in Re_i to 1500 improves the symmetry of the system; there is nearly equal penetration of the bottom and top fluid, at this stage the roll-up feature near the top of the RTM structure becomes apparent at t = 19 s. A further increase of injection of kinetic energy to Re_i = 2500 shows that it is possible to overshoot the point of symmetry, in this case the top fluid penetrates farther than the bottom ($t = 5\ s$) thereby shifting the RTM structure to the right side of the cavity at t = 19 s; the penetration of the lower density fluid into the heavier fluid at right hand side underneath the RTM structure is evident. The kinetic energy injected in the flow due to the increase of Re_i causes local deformation of the interface which modifies the sharp density concentration front at $t = 5\ s$. These experiments show that the ratio of potential to injected kinetic energy for which symmetry is approached lies in the range of $0.64 \le PE_o / KE_{iU} \le 1.38$ in which the maximum value corresponds to $Re_i = 1500$ for the range of $1500 \le \mathrm{Re}_i \le 2500$.

2. RTM fronts

For high Grashof Gr = 2.69×10^7 or Peclet Pe = 8.97×10^{10} numbers, the overturning motion that results in unstable density stratification and produces an ideal condition for the growth of a single wavelength Rayleigh-Taylor instability, unfolds to RTM fronts with fractal structures that contain small length scales, analogous to RT driven fronts[35]; these RTM fronts are shown in Fig. 5 for $Re_i = 5000$ at $t = 2.6\ s$ and $Re_i = 10000$ at $t = 2.4\ s$. The increase in intensity of the flow field causes a cascade to small length scales that show self-similar structures at smaller and smaller length scales. An increase to $Re_i = 20000$ shows the approach to symmetry of the interface structure at early times at $t = 2.0\ s$ for maximum injected impulsive kinetic energy with the ratio of potential to kinetic energy of $PE_o / KE_{iU} = 2.12$; this is analogous to the diffused interface for $Gr = 3.16\times10^6$ at equivalent Re_i that occurred for a lower initial potential energy with a ratio of $PE_o / KE_{iU} = 0.25$ showed in Fig. 3(b).

In comparison to Gr = 3.16×10^6 which requires $\mathrm{Re_i}$ O (10^3) to approach symmetry, a decade increase in Gr requires similar increase to $\mathrm{Re_i}$ O (10^4); in search for symmetry we increased the impulsive velocity from $U_o = 10\ cm/s$ or Re_i = 5000 to $U_o = 40\ cm/s$ or Re_i = 20000 shown in Fig. 5. The development of a gravity current that yields frontogenesis is shown for $Re_i = 5000$ at t = 0.4 s prior to overturning motion. The effect of asymmetry is most pronounced for $Re_i = 5000$ as the density current penetrates a substantial portion of the bottom of the cavity whereas the top of the cavity is nearly motionless where the interface configuration is similar to a miniscal shape. The overturning motion that yields RTM front ($t = 2.6\ s$) with the generic property of self-similar structures of whorls within whorls, has also been predicted by the computational model[6] for Gr O (10^7). However, imposed symmetry in the computational model, results in internal collision of the RTM fronts, whereas asymmetry in the experiments causes a relative displacement between the RTM fronts resulting in shear motion.

As Re_i increases to 10,000, there is further approach to symmetry based on the distance of the penetrating front near the top and bottom of the cavity at t = 0.4 s; the interface configuration shows a mixed mode instability with impulsive RT instability at the lower region and KH waves in the upper region. The overturning motion at $t = 2.4\ s$, yields localized small scale RTM

structures superimposed on the large scale structure that shows self-similar patterns. The RTM fronts with the attribute of self-similar small scale structures embedded within a larger structure indicate the presence of length scales that can possibly approach turbulence length scales. These length scales are potentially analogous to the small scale structures in Rayleigh-Taylor turbulence[36,37, 61]; analogous dissipative structures occur in turbulent round jets, as shown in Ref. 62.

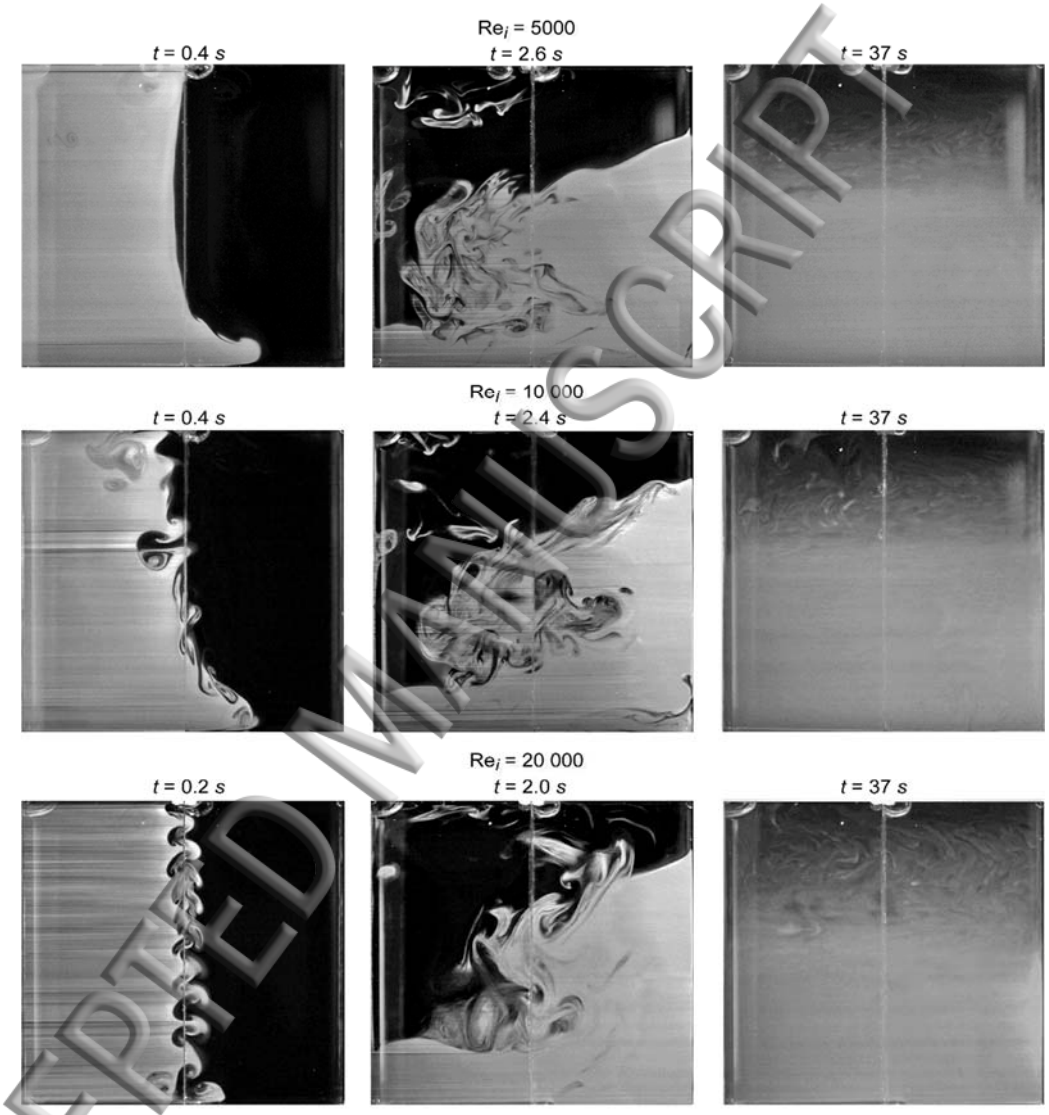

FIG. 5. Transition to RTM fronts for an increase to Gr = 2.69×10^{7} or Pe = 8.97×10^{10} shown for Re_i = 5000 at t = 2.6 s, and Re_i = 10000 at t = 2.4 s; and evolution of short wavelength impulsive Rayleigh-Taylor instability that generates the Richtmyer-Meshkov instability over short time scale t = 0.2 s for increasing impulsive Reynolds number Re_i = 20000 for Ar = 0.2 showing approach to symmetry of a diffused interface at t = 2 s.

Interface characteristics with nearly equi-penetrating fronts or mushroom structures for $Re_i = 20{,}000$ at t = 0.2 s are analogous to shock-driven RT instability or the Richtmyer-Meshkov instability[50,63]; similar instability mechanism occurs for the impulsive velocity-driven RT instability of our experiments as the shock-driven RT instability in compressible flow and the impulsive acceleration RT instability in incompressible nonhomogeneous liquids—the interaction of the vertical pressure gradient across the perturbed interface with the horizontal density gradient

ingates baroclinic vorticity and generates an incompressible Richtmyer-Meshkov instability. In comparison to Fig. 3(b) with $Gr = 3.16\times10^6$ and $Re_i = 20{,}000$, which showed mixed mode KH and impulsive RT instabilities at the interface for $t = 0.28$ s, the increase in buoyancy effects relative to injected impulsive kinetic energy as Gr increases to 2.69×10^7 leads to the development of shorter wavelength impulsive RT instability at $t = 0.2$ s with an increase in number of modes which spreads throughout the entire initial interface length. Comparison with linear theory shows that as nonlinearity increases for $Gr = 2.69\times10^7$, the disparity between linear theory from Eqs. (19, 20) and experiment also increases. The maximum wavelength $\lambda_m \approx 0.2cm$ predicted from linear theory is more than twice as less than the value of the experimental measurement $\lambda_{\exp} \approx 0.54cm$, and the characteristic time of evolution of the instability $n_m^{-1} \approx 0.1$s follows a similar trend with the experimental value of $t = 0.2$ s.

There is loss of memory of the short wavelength instability during overturning motion as inferred from the interface structure for $Re_i = 20{,}000$ at early times at t = 2.0 s. This is similar to the findings for $Gr = 3.16\times10^6$ at $\mathrm{Re}_i = 20000$ of a diffused interface for which RTM does not exist that occurred for high impulsive kinetic energy KE_{iU} in comparison to initial potential energy PE_o, that is, for $PE_o / KE_{iU} = 0.25$. The mixing efficiency is also increased in this limit as evidenced from the large diffusive region of the stably stratified configuration at $t = 37$ s; the increase of injected kinetic energy relative to initial potential energy showed similar effect for $Gr = 3.16\times10^6$ and $Re_i = 20{,}000$. For the range of impulsive Reynolds number $5000 \le \mathrm{Re}_i \le 20000$ for Gr = 2.69×10^7, the ratio of potential to kinetic energy lies in the range of $2.12 \le PE_o / KE_{iU} \le 11.99$; the lower bound that corresponds to $\mathrm{Re}_i = 20000$ indicates that there is a critical injected impulsive kinetic energy KE_{iU_c} for which the formation of RTM front is inhibited that occurs at high impulsive Reynolds numbers.

V. MEASUREMENT OF KINEMATICS OF THE INTERFACE

The kinematics of interface motion is quantified from the measurement of the length stretch $\mathcal{L}$(t) of the interface, width $\delta_w(t)$ of the interface, and mixing efficiency η_E; whereas its sloshing characteristic, such as its damped frequency f_d is measured experimentally from the time history of the length stretch which is compared to the theory of oscillations of two superposed liquids and to a harmonic oscillator model of interface sloshing.

A. Time history of length stretch of the interface

The Lagrangian history of the length stretch $\mathcal{L}$(t) of the interface contains the continuum mechanics of buoyancy-driven mixing. The time history of the length stretch of the interface, measured from the FFV method using image processing techniques, is shown in Figs. 6(a, b) for a selected range of aspect ratios $Ar = 0.1, 0.2, 0.5$ with impulsive Reynolds number of $Re_i = 1500$, and for $Ar = 0.04, 1.0$ with $Re_i = 2500$ and $Gr = 3.18\times10^6$. The trends of the data indicate that

This manuscript was accepted by Phys. Fluids. Click here to see the version of record.

stretching and folding of the interface during mixing is self-similar. For $Re_i = 1500$, as the aspect ratio increases from $Ar = 0.1$ ($W = 0.5$ *cm*) to $Ar = 0.2$ ($W = 1$ *cm*) there is a transition from linear to exponential length stretch of the interface, since the interface does not fold in the region $0 < Ar \leq 0.1$. The transition from asymmetry towards symmetry as the impulsive Reynolds number Re_i increases also occurs even when there is only stretching of the interface ($Ar = 0.1$) relative to the horizontal and vertical line at center of cavity, as also illustrated in Fig. 4 for $Gr = 3.7\times10^5$ with $Ar = 0.2$; beyond the maximum length stretch there is subsequent contraction of the interface toward stratification, though sloshing occurs however its amplitude is too small to be discernable in Fig. 6a for $Ar = 0.1$. For increasing aspect ratio $Ar = 0.2$, the catastrophic collision of the RTM structure with the wall causes an increase in the maximum length stretch of the interface. The variation of aspect ratio from 0.04 to 1.0, shows a transition to a nearly Gaussian distribution of the length stretch.

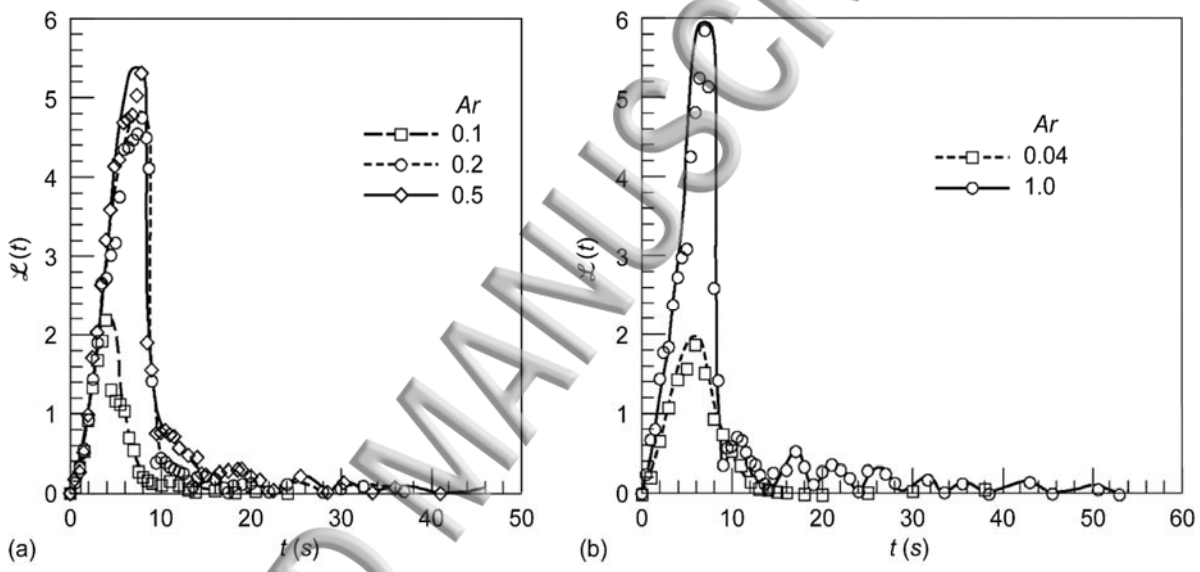

FIG. 6. Time history of length stretch of interface of $\mathcal{L}$(t), using FFV method, for increasing aspect ratio Ar at fixed Gr = 3.18×10^6, or Pe = 1.06×10^{10} (a) Re_i = 1500, (b) Re_i = 2500.

Following the breakdown of the interface from wall collision of RTM for $Ar = 0.2$, there is a sharp change in length stretch beyond its maximum $\mathcal{L}_{max}$; the interface contracts over a very short time interval in the neighborhood of 2 seconds. The wall collision of RTM caused by the overturning motion gives rise to self-induced sloshing, denoted by the zero values of the length stretch for $t > 10$ *s*. This event of sloshing generated by the flow field itself without sustained external driving force which shows only the first mode, serves as an example of self-induced sloshing between two superposed liquids, in contrast to self-induced free-surface sloshing addressed in Ref. 62 that also shows the occurrence of second mode sloshing. The exponential decay of sloshing has the characteristic of a damped harmonic oscillator. As the aspect ratio increases further to $Ar = 0.5$, there is similarity of the length stretch distribution, with a resulting increase in maximum length stretch. Similar trends are shown for $Re_i = 2500$, however at $Ar = 0.04$ there is no folding, the interface only stretches and for $Ar = 1.0$ in which the maximum length stretch occurs there is an increase in amplitude of sloshing with a slow decay; this occurs through several cycles of sloshing toward stratification.

This manuscript was accepted by Phys. Fluids. Click here to see the version of record.

1. Self-induced sloshing of the interface

The time history of the length stretch of the interface in Figs. 6(a,b) indicates that the kinematics of interface motion has two time scales. A short time scale to denote divider disturbance and resulting stretching and folding which lead to wall and internal collision, represented by $T_{SF,}$ followed by a long time scale T_f to denote settling time to the stably stratified configuration which spans $T_{SF} < t \leq T_f$. Sloshing decays over the time scale $T_{SF} < t \leq T_f$ and approximated as the long time response of the interface to initial input disturbance over the time scale $0 \leq t \leq T_{SF.}$ For the long time scale T_f, the decay rate of sloshing as shown in Figs. 6(a,b) depends on the aspect ratio and shows that as the aspect ratio increases it takes longer for sloshing to decay; this event can contribute to the overall molecular diffusion at the interface resulting in an increase in mixing width $\delta_w(t)$.

The damped natural frequency f_d is calculated from the time signal of the length stretch of the interface by averaging over the representative time interval. The characteristic trend of the damped frequency f_d of sloshing in Fig. 7 for $\mathrm{Gr} = 3.18 \times 10^6$ indicates that for $0 < Ar < 0.1$, the approximate Hele-Shaw cell configuration, the interface exhibits (Fig. 6(a)) overdamped behavior as it approaches the stably stratified configuration; thus there is a long period oscillation in the range of $0 < Ar < 0.1$. The damped frequency of sloshing for the range $0.1 \leq Ar \leq 1.0$ shows underdamped oscillation of the interface with a conditionally periodic frequency[65] as the aspect ratio increases. Though there is an increase in intensity of the flow field for $0.5 \leq Ar \leq 1.0$ due to the increase in volume with a corresponding increase in the initial potential energy of the system, the damped frequency approaches an asymptotic value.

The experimental trend of the damped frequency f_d as a function of aspect ratio Ar compares favorably to a damped harmonic oscillator model given by Eq. C4 in Appendix C which shows from scaling that the undamped natural frequency is given as,

$$\omega_n = \sqrt{n g_o (\frac{2}{L}) At} \tag{27}$$

Equation (27) indicates that the frequency scales with the square root of aspect ratio as $f_n \sim Ar^{1/2}$ when the characteristic length scale is the width L of the cavity, which is in qualitatively agreement with the trend of the experimental data in Fig. 7. Since the effective wavenumber $k_e = 2/L = 2Ar/W$ with $H=L$ is on the same order of magnitude as the first mode wavenumber $k = q\pi / \lambda$ ($\lambda = L$, $q = 1$) predicted from the theory of oscillations of two superposed fluids[66] shown below, Eq. (27) yields $\omega_n = 0.712\, rad/s$, which is on the same order as the sharp interface inviscid theory $\omega_1 = 0.893\, rad/s$ given by Eq. (29) below, for the small wavelength approximation.

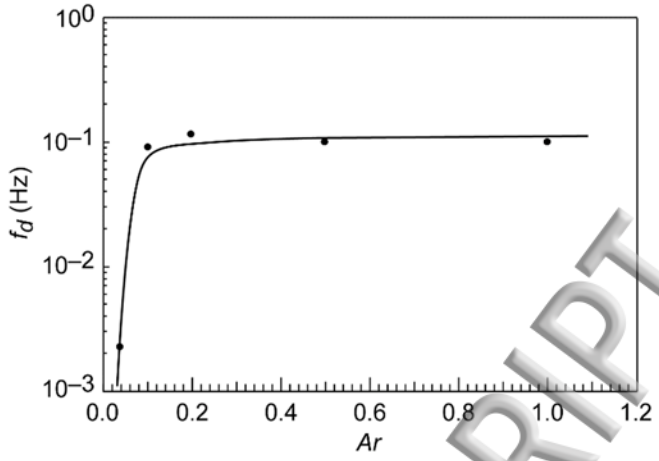

FIG. 7. Damped natural frequency f_d of sloshing as a function of aspect ratio Ar for Gr = 3.18×10^6 or Pe = 1.06×10^{10} at Re_i = 2500.

2. Superposed fluid model of sloshing

The sloshing event may be compared to the theory of oscillation of two superposed fluids with a sharp[66] and diffused[67] interface. According to the theory of surface waves in two-dimensions, the frequency ω_0 of oscillations of the common boundary ($C = 0.5$) of two superposed inviscid liquids[66] with a sharp interface which is confined vertically between horizontal planes and unbounded in the horizontal direction $L >> H$ is given by

$$\omega_0^2 = \frac{ng_o k(\rho_A - \rho_B)}{\rho_A \coth k(H/2) + \rho_B \coth k(H/2)} \tag{28}$$

in which $kH/2$ is a dimensionless wavenumber with $k = 2\pi/\lambda_0$; for small wavelength λ_0, $\coth kH/2 \to 1$, thus the natural frequency for the qth mode oscillation for our system becomes

$$\omega_q = \sqrt{ng_o(\frac{q\pi}{\lambda_0})At} \tag{29}$$

in which q is the mode number; for $Gr = 3.18\times10^6$ only first order mode $q = 1$ is observed in our experiments. If the length scale λ_0 in Eq. (29) is on the order of the width of the cavity L, it can be shown that the frequency scales as $\omega_0 \sim Ar^{1/2}$ which shows that the theoretical prediction of the dependence of frequency on the square root of the aspect ratio is also comparable with the experimental trend in Fig. 7. In contrast to the sharp interface theory of Eq. (28), Ref. 67 shows that for an interface that has a piecewise density variation with a finite interface of width δw, based on the work in Ref. 68, the frequency of oscillation ω_D for a diffused interface is given as

$$\omega_D = \sqrt{\frac{ng_o kAt}{(1+\tanh k\delta w)}} \tag{30}$$

Equation (30) reduces to Eq. (28) when the width of the interface approaches zero, $\delta w \to 0$, for small wavelength approximation. According to the theoretical prediction of Eq. (28) for a sharp interface $\omega = 0.856\, rad/s$, which is on the order of the measured experimental value ω = 0.696 rad/s for a nearly two-dimensional cavity with $Ar = 0.2$ as shown in Table III of Appendix C, whereas Eq. (29) yields $\omega_1 = 0.893\, rad/s$ which shows that the small wavelength approximation does not appreciably affect the frequency. The difference between predicted and measured value of the frequency is attributed to the neglect of viscous effects, finite interface width, and infinite extent $L \to \infty$ approximation of the theory which is not borne out in our experiments. However, for cavity size in which $\lambda \sim (1.6L)$, Eq. (29) shows that nearly equivalent agreement with theory can be obtained. On the other hand, the diffused interface model of Eq. (30) shows that $\omega_D = 0.716\, rad/s$ for a nominal interface width of $\delta w = 1\ cm$, which compares favorably with experimental measurements. The effect of a diffused interface is to effectively decrease the frequency of oscillation of the interface as the diffused width δw increases. Given the similarity between the damped harmonic oscillator model of Eq. (27) and the superposed fluid theory of Eq. (29), the natural frequency predicted from scaling arguments given by Eq. (27) of $\omega_n = 0.712\ rad/s$ falls close to the experimental value of $\omega = 0.696\ rad/s$ as shown in Table III of Appendix C.

B. Mixing width of interface and mixing efficiency

In contrast to the length stretch $\mathcal{L}(t)$ of the interface that shows a smooth variation as a function of time up to the point where sloshing occurs as shown in Figs. 6(a,b), the mixing width $\delta_w^*(t)$ of the interface in Fig. 8 shows that there exists expansion and contraction of the mixed region during the time interval of folding up to its breakdown. Initially the width increases smoothly during the stretching event 0 s < t ≤ 3 s. The interval in which folding occurs which leads to the breakdown of the RTM structure due to wall collision, 3 s < t ≤ 10 s, shows local expansion and contraction of the mixed width of the interface. The catastrophic bifurcation[6] in which the RTM structure collides with the wall, and sets-up the condition for self-induced sloshing, results in enhanced local molecular diffusion; there is a sharp increase of the mixing width in the interval 10 s < t ≤ 18 s characterizing this event. The damping of sloshing for t > 18 s which results in a stably stratified mixed region shows that the mixing width increases slowly with time and becomes limited by molecular diffusion. These results show that the mixing width varies as a power law function of time $\delta_w^*(t) \sim t^p$ with an exponent $2 < p < 3$; this is analogous to turbulent RT instability that shows a quadratic time dependence of the mixing width that scales as $\sim Atg_o t^2$ which is attributed to the short wavelength initial perturbation[52], however when a long wavelength perturbation is added to the short wavelength initial perturbation, it is noted in Ref. 52 that the quadratic time dependence ceases to be valid.

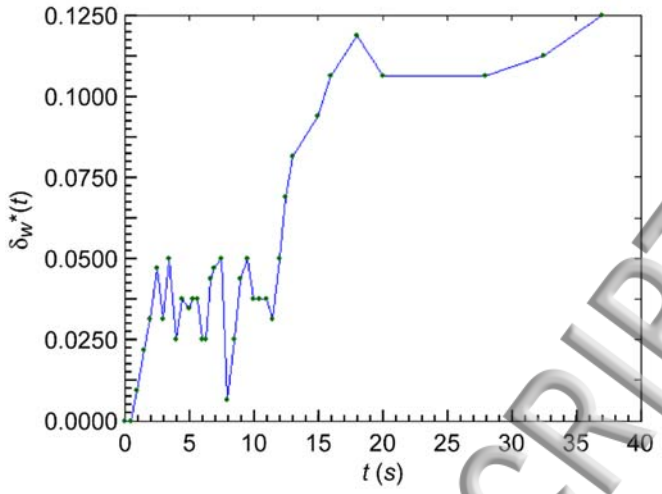

FIG. 8. Time history of interface width $\delta w^*(t)$ for Gr = 3.18×10^6 or Pe = 1.06×10^{10}, Ar = 0.2, and Re_i = 1500.

The relationship between the mixing efficiency η_E and the mixing width $\delta_w(t)$ is given by Eqs. (25,26). In this respect the mixing efficiency expressed in terms of the mixing width given by $\eta_E = \delta_w(T_f)/2h_o$, in which $t = T_f$ is the settling time for stable stratification, represents the ratio of the quasi-equilibrium mixed width $\delta_w(T_f)$ generated by the total energy input into the system relative to a uniform mixed background of width $2h_o$. The mixing efficiency can also be expressed in terms of the dimensionless mixed width $\delta^*_w(T_f)$ from Eq. (15) as $\eta_E = \delta_w^*(T_f) + \delta_{wo}/2h_o$, for a very thin interface initially $\delta_{wo}/2h_o \to 0$ and $\eta_E \to \delta_w^*(T_f)$. For practical applications Eq. (25) is used to calculate the experimental mixing efficiency; the mixing efficiency η_E, estimated from the potential energy balance model of Eq. (21), represents a measure of energy conversion between initial and final configuration of the interface which is indicative of a quasi-equilibrium state of the system, whereas $\mathcal{L}(t)$ is a measure of non-equilibrium states. In terms of a metric to characterize the kinematics of the interface, we find that the length stretch $\mathcal{L}(t)$ is a preferred descriptor of the transient kinematics of the short time events of stretching and folding. However, the long time kinematics which lead to a stably stratified configuration are conveniently described by the mixing width $\delta_w(t)$.

The effect of aspect ratio *Ar*, impulsive Reynolds number Re_i, and Grashof number *Gr* on the experimental mixing efficiency η_E, are shown in Figs. 9(a,b,c). For a fixed Grashof number *Gr* and impulsive Reynolds number Re_i, the mixing efficiency η_E increases as aspect ratio *Ar* increases (Fig. 9(a)). For $Ar \to 0$ the efficiency $\eta_E \to 0$ because there is no folding of the interface and mild stretching for $Ar = 0.04$; this region leads to the no mixing case. However, as *Ar* increases the potential energy PE_o of the system increases for fixed injected kinetic energy *KE* and results in an increase of the mixing efficiency η_E.

This manuscript was accepted by Phys. Fluids. Click here to see the version of record.

The effect of injected kinetic energy (Fig. 9(b)), for fixed *Gr* and *Ar*, is to increase the mixing efficiency by a factor of two beyond $Re_i > 4000$ due to the large injected impulsive kinetic energy KE_{iU} into the system. In the range $1000 \le \mathrm{Re_i} \le 2500$ the mixing efficiency increases as symmetry is approached which is in agreement with the observation in Ref. 7. The results show that for the maximum injected impulsive kinetic energy KE_{iU} relative to the initial potential energy PE_o with a ratio of $PE_o / KE_{iU} = 0.25$ the mixing efficiency η_E can increase by a factor of two for $\mathrm{Re}_i = 20000$. The mixing efficiency approaches an asymptotic value for $\mathrm{Re}_i \ge 10000$, this implies that the system becomes saturated or the injected kinetic energy does not appreciably affect the mixing efficiency beyond a certain threshold of Re_i. Lastly, we fix $Re_i = 2500$ and $Ar = 0.2$ to investigate the effect of *Gr* on the mixing efficiency shown in Fig. 9(c); the results show that the mixing efficiency η_E increase as *Gr* increases, which means that an increase in the initial potential energy of the system increases the mixing efficiency. Comparison of our results with the mechanical model of mixing in Part 2 denoted by the square symbol, indicate reasonable proximity with the experiment for nominal $\mathrm{Gr} = 3.16\times10^6$.

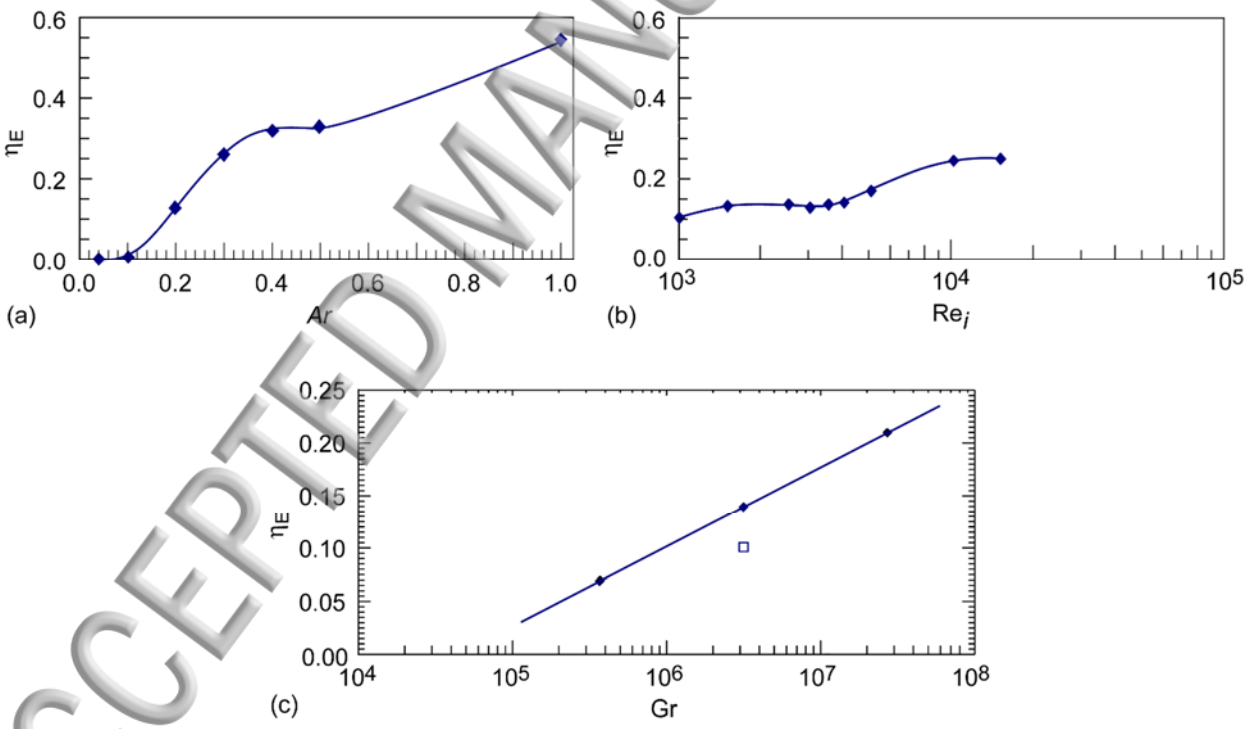

FIG. 9. Mixing efficiency η_E as a function of : (a) aspect ratio Ar for $\mathrm{Gr} = 3.18\times10^6$ or $\mathrm{Pe} = 1.06\times10^{10}$, $\mathrm{Re_i} = 2500$, (b) impulsive Reynolds number $\mathrm{Re_i}$ for $\mathrm{Gr} = 3.18\times10^6$ or $\mathrm{Pe} = 1.06\times10^{10}$, $\mathrm{Ar} = 0.2$, and (c) Grashof number Gr for $\mathrm{Ar} = 0.2$ and $\mathrm{Re_i} = 2500$; comparison to the mechanical model of mixing in Part 2 shown by the open square symbol.

VII. BIFURCATION OF INTERFACE

The local characteristics of the interface motion as a function of time show that there can be a transition from stretching to folding; under certain conditions folding gives birth to the RTM structure that can approach symmetry. We quantify the observed behavior of the interface based on its bifurcation sequence in parametric space for a given metric. The bifurcation type as a parameter unfolds is based on the geometric classification given in Ref. 69. As metric we use the maximum length stretch $\mathcal{L}_{max}$ of the interface,

$$\mathcal{L}_{max} = \mathcal{L}_{max}(Ar, Re_i, Gr, Sc) \tag{31}$$

shown in Figs. 6(a,b); the Schmidt number Sc is held fixed to reduce the parametric set. We investigate the unfolding of the solution for a reduced parametric set by varying one parameter while keeping all others fixed to find the critical parametric space

$$\Lambda_c = \Lambda_c(Ar_c, Re_{ic}, Gr_c) \tag{32}$$

whose loci of points in a plane represent either a transition from stretching to folding or asymmetric to nearly symmetric RTM structure; the parametric space can also be expressed in terms of the critical Peclet number as $\Lambda_c = \Lambda_c(Ar_c, Re_{ic}, Pe_c)$. The critical values are used to define critical boundaries on a plane for which a particular characteristic feature of the solution exists, that can also be used as operational curves. The effect of multiple parameter variation is analogous to a mathematical experiment on the first variation[70] of the initial potential energy δPE_o and injected impulsive kinetic energy δKE on a virtual change of the parametric space, owing to a perturbation of the total initial energy δE_{To}. Since we use two different experimental systems to measure the length stretch $\mathcal{L}(t)$ of the interface, we contrast the difference between the two measurements that used FFV and PLIF methods.

A. Effect of initial potential energy perturbation

1. Variation of Ar

In order to form a global picture in parametric space we consider the bifurcation of $\mathcal{L}_{max}$ as a function of aspect ratio Ar, impulsive Reynolds number Re_i, and Grashof number Gr or Peclet number Pe which represents a co-dimension three problem; the Peclet number $Pe = GrSc$ is used interchangeably with the Grashof number as the control parameter. The effect of the Schmidt number Sc is subsequently taken into account by considering liquid mixtures with a range in thermophysical properties as shown in Table I of Appendix A. The bifurcation point in parametric space can be perturbed through variation of the total initial energy δE_{To} of the system consisting of its potential energy $PE_o = C_o ArGr$ and injected impulsive kinetic energy $KE = C_o Ar\,\mathrm{Re}_i^2$ from Eqs. (B3-B5) of Appendix B, where the constant $C_o = 1/2\bar{\rho}L\bar{v}^2$.

We first consider the effect of the initial potential energy perturbation δPE_o on the variation of aspect ratio δAr and Grashof number δGr. The variation in aspect ratio δAr represents perturbation of the initial potential energy δPE_o of the system owing to a change in volume, in which $\delta PE_o = C_o Gr\delta Ar$ for fixed Gr

This manuscript was accepted by Phys. Fluids. Click here to see the version of record.

and constant C_o. Since the initial potential energy drives the characteristics of mixing quantified by $\mathcal{L}_{max}$, we consider the effect of a variation of the aspect ratio on $\mathcal{L}_{max}$ to find the critical aspect ratio. Figure 10(a) shows that as the cavity varies from an approximate Hele-Shaw cell to a three dimensional configuration the critical aspect ratio separates the region of stretching from folding, and the length stretch approaches an asymptotic value. For fixed $Gr = 3.18 \times 10^6$ or $Pe = 1.06 \times 10^{10}$, the interface undergoes a supercritical bifurcation in the neighborhood of $Ar_c = 0.15$ which separates the stretching and folding region. In the region where the interface stretches, the short-lived coherent RTM structure shown in Figs. 3(a,c) does not exist; however, the RTM structure occurs at the bifurcation point.

The bifurcation of the interface as a function of Ar and Gr requires that the impulsive Reynolds number Re_i should be a fixed optimum value. We show in Fig. 10(a) the implication of operating below an optimum value of Re_i. Ideally Re_i should be selected such that there is negligible effect on $\mathcal{L}_{max}$; operating below an optimum Re_i implies that there is an effect on the length stretch beyond the critical aspect ratio as shown by contrasting the results for $Re_i = 1500$ and 2500. As the aspect ratio of the cavity increases, the initial potential energy available to fold the interface also increases, it becomes necessary to increase the impulsive velocity of the divider so as to minimize effect on the length stretch of the interface. Even though one can operate at $Re_i = 1500$ for $Ar < 0.5$, as $Ar \rightarrow 1$ the length stretch decrease shown by the data in Fig. 10(a) is caused by the delay of the divider motion which inhibits the stretching and folding event; the increase of the impulsive Reynolds number to $Re_i = 2500$ prevents potential interface contraction effects caused by delay of the divider.

The bifurcation of the interface for various fixed Gr as Ar is varied, shown in Fig. 10(b) in relation to $Gr = 3.18 \times 10^6$ or $Pe = 1.06 \times 10^{10}$ for fixed $Re_i = 2500$, indicates that for a given critical aspect ratio Ar_c there is a fixed critical initial potential energy PE_{oc} for transition from stretching to folding. The effect of a variation of δPE_o on the variation of aspect ratio δAr for fixed Grashof numbers Gr, shows that an increase to $Gr = 2.69 \times 10^7$ or $Pe = 8.97 \times 10^{10}$ requires a decrease in the critical aspect ratio to $Ar_c = 0.08$. On the other hand, as Gr decreases to $Gr = 3.7 \times 10^5$ or $Pe = 1.23 \times 10^9$ the system compensates for the lower energy available to drive folding by an increase in critical aspect ratio to $Ar_c = 0.3$; these trends verify the direct relationship of Gr and aspect ratio δAr given by δPE_o. For $Gr = 3.7 \times 10^5$ as Ar varies from 0.04 to 1, $\mathcal{L}_{max}$ increases from 2.0 to 7.6; comparison with the computational model[6] shows $\mathcal{L}_{max} = 7.2$ which indicates that the 2D approximation of the cavity is approached asymptotically.

2. Variation of Gr

We consider the effect of perturbing the initial potential energy δPE_o through a variation of δGr for a fixed Ar, which implies $\delta PE_o = C_o Ar \delta Gr$, to determine the critical Grashof number that separates stretching and folding. In Fig. 10(c) we show that a supercritical bifurcation occurs in the neighborhood of $Gr_c = 4.0 \times 10^5$ which separates stretching from folding for a fixed aspect ratio of $Ar = 0.2$; this critical value is on the same order of magnitude as predicted by the computational model[6] in which $Gr_c = 3.0 \times 10^5$ showed the birth of the RTM structure. The difference between experiment and model is attributed to initial condition effects due to divider disturbance which is not taken into account in the 2D model, and the 2D approximation of the cavity. The impulsive

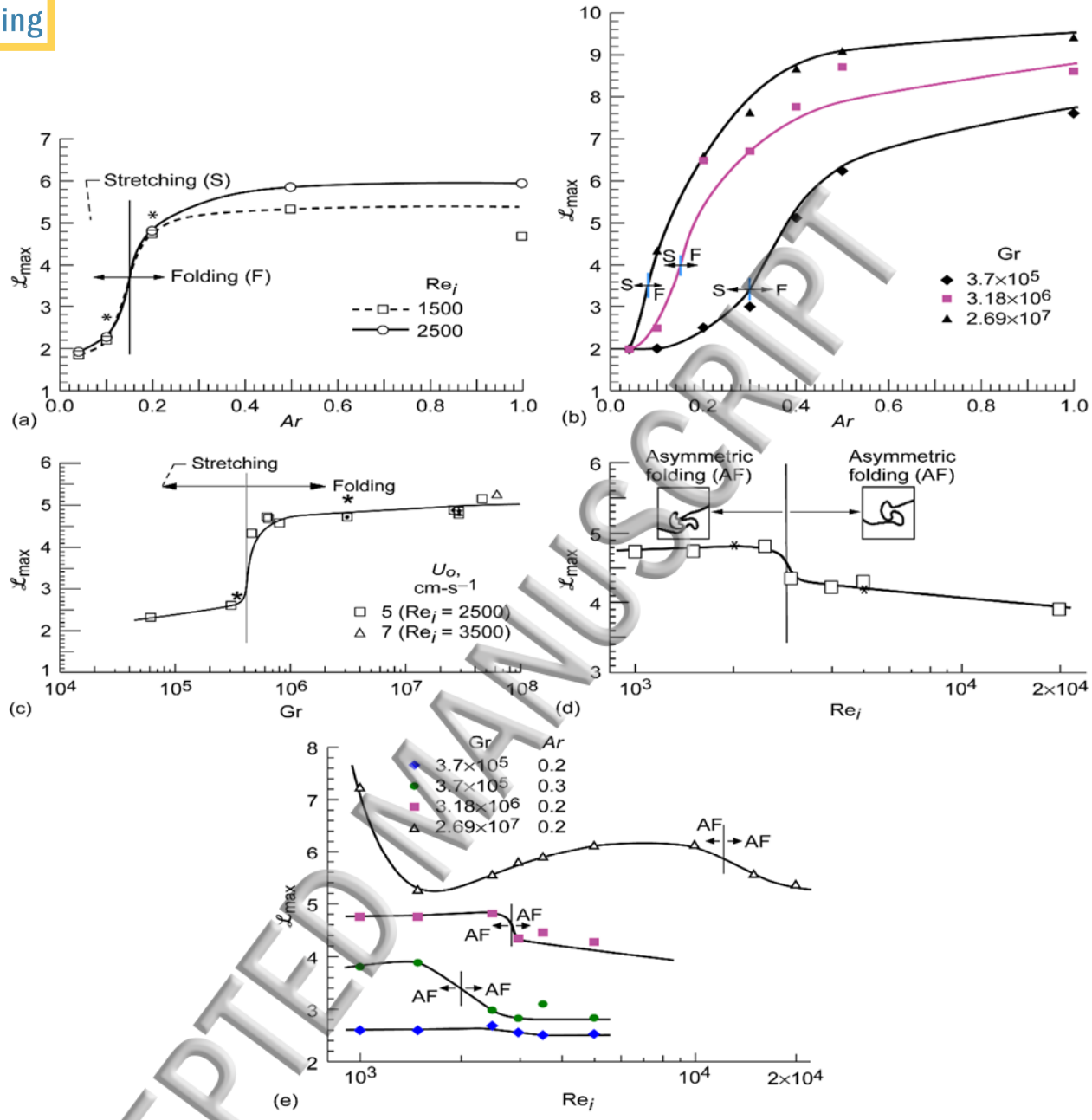

FIG. 10. Local bifurcation sequence of the maximum length stretch $\mathcal{L}_{max}$ of the interface as a function of its parametric space (Ar, Gr, Re_i) for Sc = 3333. (a) Bifurcation of interface $\mathcal{L}_{max}$ showing transition region from stretching to folding as aspect ratio Ar of cavity increases for various impulsive Reynolds number Re_i for Gr = 3.18×10^6 or Pe = 1.06×10^{10} using the FFV method, for comparison * corresponds to PLIF method. (b) Effect of variation of Grashof number Gr on bifurcation point of $\mathcal{L}_{max}$, represented by the vertical bars, as aspect ratio Ar increases for Re_i = 2500 using the PLIF method. (c) Bifurcation of interface as Grashof number Gr increases for fixed aspect ratio Ar = 0.2 showing transition from stretching to folding using FFV method, data corresponding to ⊡ were also taken from microgravity experiments in Ref. 45, for comparison * corresponds to PLIF method. (d) Effect of increasing the impulsive Reynolds number Re_i on interface bifurcation showing that the approach to symmetry lies between asymmetric folding using FFV method, Gr = 3.18×10^6 or Pe = 1.06×10^{10}, Ar = 0.2; (e) Effect of variation of Grashof number Gr on the critical impulsive Reynolds number Re_i, using PLIF method.

velocity was kept fixed at $U_0 = 5\ cm/s$, with the exception of data points obtained in microgravity environment[45] and $Gr = 6.36\times10^7$ or $Pe = 2.12\times10^{11}$, for cases 4-7 in Table I of Appendix A. For the highest Grashof number $Gr = 6.36\times10^7$, it is necessary to increase the impulsive velocity to $U_0 = 7\ cm/s$ so that $\mathcal{L}_{max}$ would not be affected by delay of divider motion as we had previously discussed. The effect of increasing the aspect ratio, can also be inferred from the relation $\delta PE_o = C_o Ar \delta Gr$, which indicates that the critical Grashof number would decrease, whereas a decrease in aspect ratio would increase Gr_c.

2. Variation of Gr

We consider the effect of perturbing the initial potential energy δPE_o through a variation of δGr for a fixed Ar, which implies $\delta PE_o = C_o\, Ar \delta Gr$, to determine the critical Grashof number that separates stretching and folding. In Fig. 10(c) we show that a supercritical bifurcation occurs in the neighborhood of $Gr_c = 4.0\times10^5$ which separates stretching from folding for a fixed aspect ratio of $Ar = 0.2$; this critical value is on the same order of magnitude as predicted by the computational model[6] in which $Gr_c = 3.0\times10^5$ showed the birth of the RTM structure. The difference between experiment and model is attributed to initial condition effects due to divider disturbance which is not taken into account in the 2D model, and the 2D approximation of the cavity. The impulsive velocity was kept fixed at $U_0 = 5\ cm/s$, with the exception of data points obtained in microgravity environment[45] and $Gr = 6.36\times10^7$ or $Pe = 2.12\times10^{11}$, for cases 4-7 in Table I of Appendix A. For the highest Grashof number $Gr = 6.36\times10^7$, it is necessary to increase the impulsive velocity to $U_0 = 7\ cm/s$ so that $\mathcal{L}_{max}$ would not be affected by delay of divider motion as we had previously discussed. The effect of increasing the aspect ratio, can also be inferred from the relation $\delta PE_o = C_o Ar \delta Gr$, which indicates that the critical Grashof number would decrease, whereas a decrease in aspect ratio would increase Gr_c.

The microgravity data in Fig. 10(c) for the high Grashof number cases (4,5,7) in Table I of Appendix A were taken at a g-level of $10^{-6} g_o$ [45], thus reducing the Grashof numbers to 3.18, 26.9 and 29.6 respectively. Those results[45] show that the interface is stabilized, therefore does not stretch and remains frozen in the vertical configuration. Thus the length stretch $\mathcal{L}(t)$ approaches zero and provides the low limit in Grashof number which is in agreement with the computational model[6] that shows $\mathcal{L}_{max} = 0$ for $Gr \leq 37.3$. Experiments in the neighborhood of $0 < Gr < 6\times10^4$ are challenging to perform on the ground; a low gravity environment can be used advantageously to investigate this range of parameters. As we had pointed-out we employed two methods to measure the length stretch of the interface, FFV and PLIF; the data in Figs.10(a,c,d) and Figs. 10(b,e) contrast respectively the difference between FFV and PLIF methods for measuring the length stretch. Owing to higher resolution afforded by the PLIF method the maximum length stretch $\mathcal{L}_{max}$ differs between the two methods beyond the bifurcation point, however, the shape of $\mathcal{L}(t)$ is not appreciably affected; thus the same trend as shown in Figs. 6(a,b) is represented by the PLIF method except for a change in magnitude of $\mathcal{L}_{max}$. We find that below or in the neighborhood of the bifurcation point the two methods show good agreement, for reference we show corresponding data points using PLIF in Figs. 10(a,c,d) for points below and above the bifurcation point denoted by the symbol *.

This manuscript was accepted by Phys. Fluids. Click here to see the version of record.

B. Effect of injected kinetic energy perturbation

1. Variation of Re_i

The length stretch may be perturbed through a variation of the initial potential energy δPE_o or a variation of the injected impulsive kinetic energy δKE. The variation of the injected kinetic energy δKE given as $\delta KE = 2C_o Ar \,\mathrm{Re}_i \,\delta \mathrm{Re}_i$ indicates Grashof number independence for fixed aspect ratio, and an aspect ratio dependence as $\delta KE = C_o \,\mathrm{Re}_i^2 \,\delta Ar$ for fixed Re_i. The unfolding of the solution as the impulsive velocity or Re_i increases shows in Fig. 10d that the RTM structure bifurcates from asymmetric to a nearly symmetric structure at a critical impulsive Reynolds number $Re_{ic} = 2800$ for $Gr = 3.18\times10^6$ and becomes asymmetric again as Re_i increases. This sequence of events indicate a change in the structural stability of the RTM structure as the impulsive Reynolds number increases; structural stability in the sense that the bifurcation from asymmetry to near symmetry is caused by perturbation of the flow field owing to injected impulsive kinetic energy into the system. In relation to the bifurcation point, asymmetric folding gains stability as the system approaches symmetric folding for increasing Re_i from the left or below the bifurcation point and loses stability to asymmetric folding for increasing Re_i on the right or above the bifurcation point.

The fundamental issue being the optimum impulsive velocity $U_o(\%)$ for which the injected impulsive kinetic energy in the system compensates the initial potential energy so as to approach symmetry. The bifurcation point which represents the approach to symmetric folding, bounded on the left by asymmetric folding as Re_i decreases and on the right by asymmetric folding as Rei increases, indicates that there is a narrow parametric space for which the approach to symmetry occurs. Even though the variation of δKE is independent of Gr, and the variation of δPE_o is independent of Re_i, their combined interaction shown by the maximum length stretch $\mathcal{L}_{max}$ in Fig. 10(e) indicates an inverse relationship between the injected impulsive kinetic energy to approach symmetry and available potential energy for folding. The inverse relationship between δRe_i and Gr on $\mathcal{L}_{max}$ indicates that as Re_{ic} increases it is necessary to increase the Grashof number to approach symmetric folding and shows relative to $Gr = 3.18\times10^6$, that the critical impulsive Reynolds number decreases to $Re_{ic} = 2.0\times10^3$ for $Gr = 3.7\times10^5$, likewise when Gr increases to $Gr = 2.69\times10^7$ the critical $Re_{ic} = 1.25\times10^4$ also increases. In contrast to the other cases, for $Gr = 2.69\times10^7$ $\mathcal{L}_{max}$ increases for $Re_i < 1500$; this limiting data point which is outside of our immediate interest shows that for low injected impulsive kinetic energy in relation to the initial potential energy, the wake of the divider exhibits the characteristic interface shape of meniscal breakoff[71] illustrated in Fig. 5 for $Re_i = 5000$ at $t = 0.4$ s, due to attachment of the interface to the trailing edge of the divider in which there is a common line of contact between the liquid-liquid interface.

This manuscript was accepted by Phys. Fluids. Click here to see the version of record.

(c) Critical boundaries

The variation of the initial potential energy δPE_o and the injected kinetic energy δKE that yields the critical parametric space Λ_c can be used to identify the co-existence of folding and the approach to symmetry in the system. We have shown that the initial potential energy can be perturbed by either a variation in aspect ratio δA (Figs. 10(a,b)) or a variation in δGr (Fig. 10(c)), which yield the critical parameters Ar_c and Gr_c. A succinct representation of the findings is shown in Fig. 11(a) which shows the critical boundary in the control space (Gr, Ar_c) that separates stretching and folding. Similarly we also showed that the injected kinetic energy can be perturbed δKE by a variation in impulsive Reynolds number δRe_i (Figs. 10(d,e)) which yields the critical Re_{ic}. Likewise the control space (Gr, Re_{ic}) in Fig. 11(b) shows succinctly that the critical boundary, that represents the transition from asymmetric to nearly symmetric folding, has a narrow parametric range since asymmetry lies on either side of the critical boundary. The co-existence of folding and the approach to symmetry can be represented by the critical boundary in the space of Re_{ic} and Ar_c shown in Fig. 11(c).

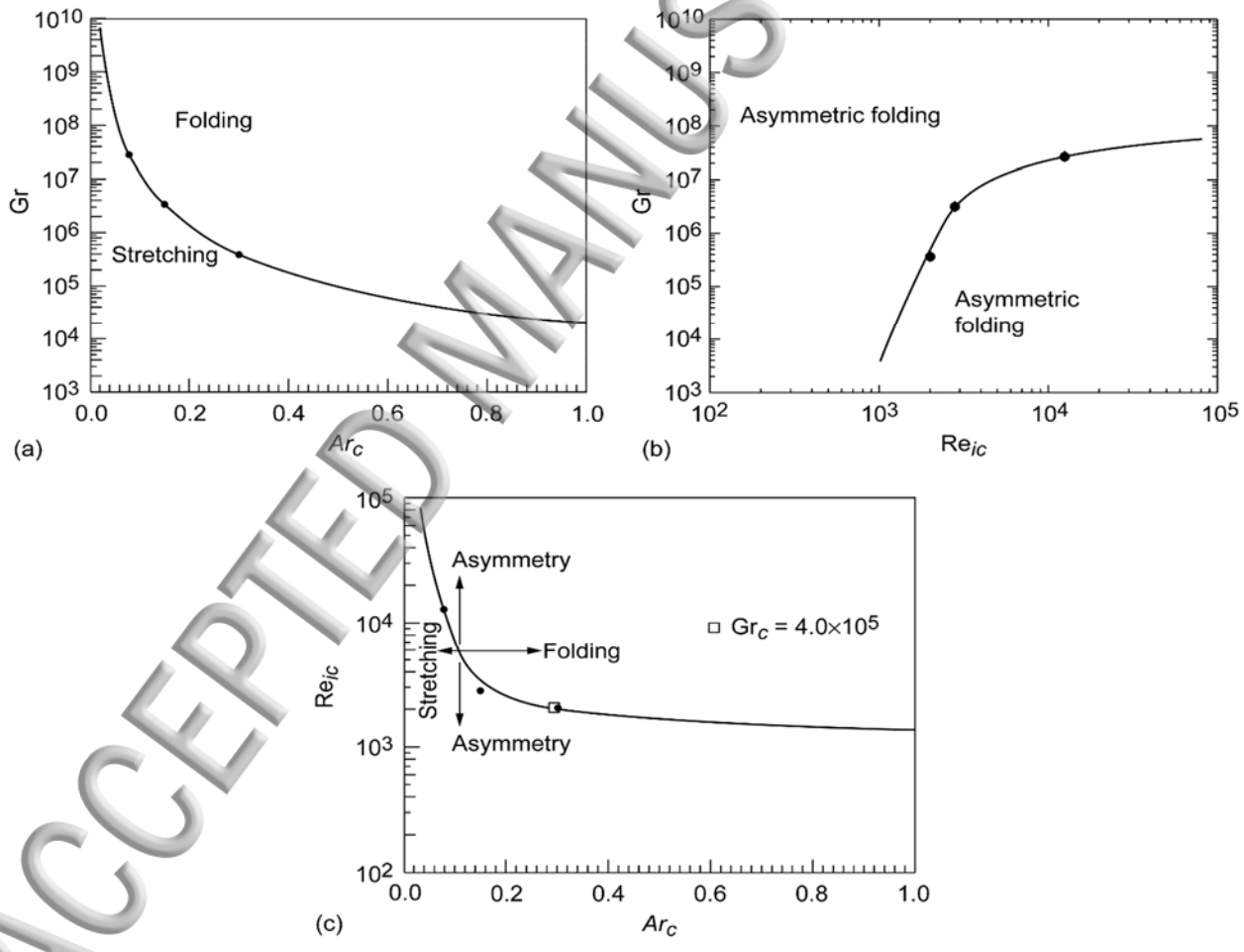

FIG. 11. The co-existence of folding and approach to symmetry denoted by critical boundaries for variation of the parametric space (Gr, Ar_c, Re_{ic}) with Sc = 3333. The critical boundary which: (a) separates stretching and folding in the control space of Gr and Ar_c; (b) shows that the approach to symmetry lies between asymmetric folding in the control space of Gr and Re_{ic}; (c) satisfies both criteria for folding and the approach to symmetry in the control space of Re_{ic} and Ar_c .

This manuscript was accepted by Phys. Fluids. Click here to see the version of record.

The critical boundaries signify that for a given Grashof number there are unique values of Re_{ic} and Ar_c for which folding occurs and symmetry is approached. The operational application of the critical boundaries denoted by Figs. 11(a,b,c) which represents regions of 2D flow, may be illustrated as follows: for a given Grashof number Gr there is a critical aspect ratio Ar_c for folding (Fig. 11(a)) as well as a critical impulsive Reynolds number Re_{ic} (Fig. 11(b)) for the approach to symmetry; folding gives birth to the RTM structure, in order for RTM to approach symmetry then there is a unique combination of (Re_{ic}, Ar_c) that satisfies the criterion for folding and the approach to symmetry. For example the critical Grashof number of $Gr_c = 4.0\times10^5$ shown in Fig. 10(c) which is obtained from $Ar = 0.2$ and $Re_i = 2500$ does not necessarily imply that the RTM structure is nearly symmetric; approach to symmetry can be found from the corresponding critical Ar_c and Re_{ic} from Figs. 11(a,b), that shows $Ar_c = 0.29$ and $Re_{ic} = 2030$ which is denoted in Fig. 11(c) as a reference value. Therefore the critical boundary denoted in the space (Re_{ic}, Ar_c) signifies the operational curve that satisfies both criteria, hence the co-existence of folding and the approach to symmetry.

The operational application of Figs. 11(a,b,c) can be used to find the critical Grashof or Peclet number for folding to occur at $Ar = 0.2$ as well as its critical impulsive Reynolds number Re_{ic} to approach symmetry. Since the birth of folding is shown in Fig. 4 to occur during the transition from $Ar = 0.2$ to $Ar = 0.3$ at $Gr = 3.7\times10^5$ or $Pe = 1.23\times10^9$, the data point for $Ar = 0.3$ represents the approximate minimum aspect ratio for which folding occurs for the given Grashof or Peclet number. However, it is the corresponding critical Grashof or Peclet number for which folding occurs at $Ar = 0.2$ that is of interest. The bifurcation diagram in Fig. 11(a) shows that at $Ar_c = 0.2$ folding occurs for the critical value of $Gr_c = 1.33\times10^6$ or $Pe_c = 4.43\times10^9$, and the critical Re_{ic} for the RTM structure to approach symmetry is $Re_{ic} = 2200$ from Fig. 11(b). In contrast, for decreasing critical Grashof number $Gr_c = 4\times10^5$, it is shown in Fig. 11(a) that there is an increase in critical aspect ratio to $Ar_c = 0.29$; the trend of the data indicates that the critical Gr_c lies along the critical boundary in Fig. 11(c) and Gr_c decreases along the critical boundary as the critical aspect ratio increases. The critical value $Gr_c = 1.33\times10^6$ represents a limiting minimum value for the existence of folding at the critical aspect ratio $Ar_c = 0.2$. The critical boundary in Fig. 11(c) serves to demarcate the region which separates stretching and folding as well as the approach of asymmetric RTM structure to near symmetry.

D. Scaling of length stretch based on bifurcation diagram

The bifurcation sequences shown in Figs. 10(a-e) may be used to construct a predictive model for the maximum length stretch $\mathcal{L}_{max}$ of the interface. We investigate a power law model[70] for the maximum length stretch of the form

$$\mathcal{L}_{max} \sim Gr^{\gamma} Ar^{\zeta} \mathrm{Re}_i^{\vartheta} Sc^{\kappa} \tag{33}$$

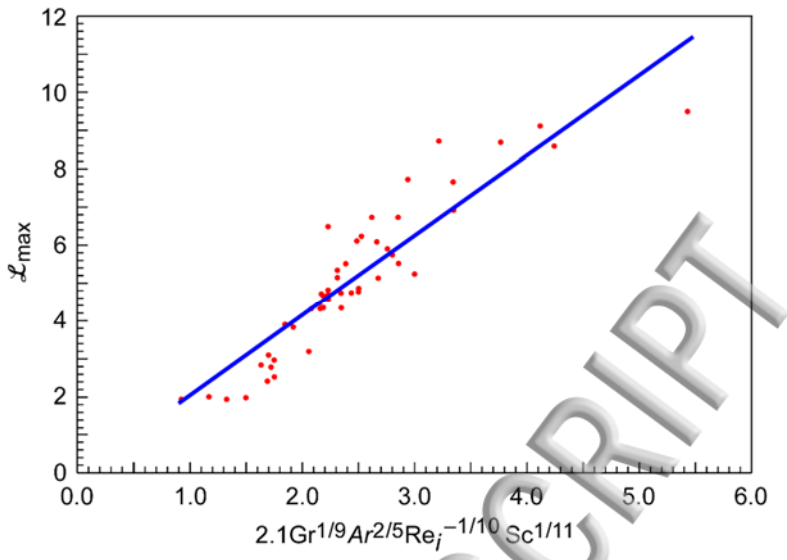

FIG. 12. The maximum length stretch $\mathcal{L}_{max}$ as a function of the parametric space of the system (Gr, Ar, Re_i, Sc) showing power law relationship with system parameters.

For the range of experimental parameters shown in Table I of Appendix A, we have investigated case 4 ($Gr = 3.18 \times 10^6$) for microgravity[45] condition $ng_o = 10^{-6} g_o$ ($Gr = 3.18$) as well as cases 5 and 7, which provide limiting data points. Rectification of the data in Table I of Appendix A for $\mathcal{L}_{max}$ shows in Fig. 12 that its functional relationship using the power law model of Eq. (33) can be represented by,

$$\mathcal{L}_{max} = 2.1 Gr^{1/9} Ar^{2/5} \mathrm{Re}_i^{-1/10} Sc^{1/11} \tag{34}$$

for the following limits: $3.18 \le Gr \le 6.36 \times 10^7$ or $1.06 \times 10^4 \le Pe \le 2.12 \times 10^{11}$, $0.04 \le \mathrm{Ar} \le 1.0$, $100 \le \mathrm{Re}_i \le 2 \times 10^4$, and $Sc >> 1$. Since it is not practical to vary the range of variables continuously, the power law model allows prediction over a continuous range of parameters within the above intervals where experimental data is lacking. According to the above model the aspect ratio and Grashof number have the dominant functional relationship as they govern transition from stretching to folding; the impulsive Reynolds number which governs the structural stability of folding, transition from asymmetry to near symmetry, shows an inverse functional relationship. The Schmidt number incorporates the effect of viscosity jump as well as molecular diffusion. A more common parameter over the Grashof number used to characterize mixing is the Peclet number that represents the ratio of mass transport by convection to that of molecular diffusion. An alternative functional relationship for $\mathcal{L}_{max}$ can be expressed as a function of Pe by setting $\gamma = \kappa$ in Eq. (33) to yield

$$\mathcal{L}_{max} \sim Pe^{\chi} Ar^{\zeta} \mathrm{Re}_i^{\vartheta} \tag{35}$$

The data fit to this model indicates

$$\mathcal{L}_{\max} = 2.4\, Pe^{1/10} Ar^{2/5} \mathrm{Re}_i^{-1/10} \tag{36}$$

and shows greater scatter of the data when superimposed on Fig. 12 which seems to indicate that the Schmidt number parameter is independent and can be used as an additional parameter. In analogy to our model experiment, application to chemical reaction with fast reactant kinetics in which the interface acts as a boundary between segregated reactants[73] show an analogous length of reaction interface that scales as $Pe^{1/8}$ for the regime which is controlled by kinematics.

VII. SUMMARY AND CONCLUSIONS

The mixing characteristic of two miscible viscous liquids driven by transient buoyancy-induced flows is investigated from measurements of its length stretch and interface width that contain the continuum mechanics of mixing, stemming from the Lagrangian history of the interface motion measured using full-field view method (FFV) and planar laser-induced fluorescence (PLIF). Buoyancy-driven mixing occurs through stretching and folding of the interface, generated by an overturning motion that results in unstable density stratification and produces an ideal condition for the growth of a single wavelength Rayleigh-Taylor instability with an asymmetric pairwise spike and bubble configuration exhibiting the Rayleigh-Taylor morphology (RTM). The late stage of RTM unfolds to an internal breakwave and its breakdown occurs through wall and internal collision which sets up the condition for self-induced sloshing that decays exponentially with a resulting diffusive region at the interface indicating local molecular diffusion.

The approach to symmetry of the short-lived coherent RTM structure is dependent on the injected kinetic energy in the system characterized by an impulsive Reynolds number while the transition from stretching to folding is dependent on initial potential energy characterized by Grashof or Peclet number. The stretching event shows density currents that cause frontogenesis owing to the sharp density front; while, the folding event shows a transition from a smooth RTM structure to RTM fronts with fractal structures that contain small length scales for increasing Grashof or Peclet number. The dependence of length stretch on aspect ratio for fixed Grashof or Peclet number showed a transition to a nearly Gaussian distribution for increasing aspect ratio which indicated self-similarity of buoyancy-driven mixing.

The interface is characterized by a co-dimension three bifurcation of the maximum length stretch in parametric space—Grashof or Peclet number, aspect ratio, and impulsive Reynolds number—for a geometric range from an approximate two-dimensional Hele-Shaw cell to a three-dimensional cavity. In particular for fixed aspect ratio the impulsive Reynolds number quantifies the approach to symmetry, from the initial condition which is set through the impulsive perturbation of the divider motion that has the characteristics of transient Couette-Poiseuille flows for the short time scale; whereas, the Grashof or Peclet number determines the control space that separates stretching and folding. The bifurcation of the length stretch of the interface in parametric space indicates that the birth of RTM occurs through a supercritical bifurcation as Grashof or Peclet number increases for fixed aspect ratio which is in agreement with the approximate computational model. The maximum length stretch scales as a power law function of the control

parameters—Grashof or Peclet number, aspect ratio, impulsive Reynolds number, and Schmidt number—and shows reasonable agreement with experimental data. The critical control space for the co-existence of folding and the approach to symmetry for the short-lived coherent RTM structure depends on the critical impulsive Reynolds number, and aspect ratio for a given Schmidt number at critical Grashof or Peclet number.

Low impulsive Reynolds numbers generate Kelvin-Helmholtz (KH) instability at the interface for the short time scale and affect the approach to symmetry. Whereas high impulsive Reynolds numbers excite short wavelength instability initially due to the (impulsive) Rayleigh-Taylor (RT) instability mechanism, that diffuses the interface and inhibits the formation of the RTM structure when the injected impulsive kinetic energy becomes comparable to the initial potential energy, and serves as an analog to shock-induced RT instability exemplified by the Richtmyer-Meshkov instability. The instability mechanism for the impulsive velocity-driven RT instability of our experiments, is similar to the shock-induced RT instability in compressible flow and the impulsive acceleration RT instability in incompressible nonhomogeneous liquids—and showed that the interaction of the vertical pressure gradient across the perturbed interface with the horizontal density gradient creates baroclinic vorticity and generates an incompressible Richtmyer-Meshkov instability.

In particular the initial perturbation of the interface and flow field for low impulsive Reynolds numbers that generates KH instability causes kinks at the interface, which grow into deep fingers during overturning motion and unfold into local whorl structures that merge and self-organize into large length scale RTM structure. However an increase in Grashof or Peclet number causes a cascade to small length scales that produce RTM fronts with self-similar structures at smaller and smaller length scale. Following breakdown of the RTM structure, the exponential decay of sloshing occurs over a narrow frequency band for aspect ratios that yield folding and results in a stably stratified configuration. From the time history of the length stretch, the finding that the damped frequency of sloshing increases as the square root of aspect ratio for fixed Grashof or Peclet number is comparable to the normalized frequency from the damped harmonic oscillator model of interface sloshing and the characteristic frequency predicted from inviscid theory of two superposed fluids. The observed interface structure and its characterization indicate that for a critical Grashof or Peclet number, two-dimensional approximation applies in the neighborhood of the critical aspect ratio and impulsive Reynolds number that separate respectively stretching and folding, and transition from asymmetry to near symmetry. In addition, our experimental model—with the distinguishing feature of an impulsive-velocity initial condition at the interface between two nonhomogeneous liquids—shows a novel method for generating short time Richtmyer-Meshkov instability in incompressible liquids.

Acknowledgements

We acknowledge Code UG of NASA for support under Grant No. NAG3-2443. We thank one of the reviewers for constructive comments that sharpened the presentation.

This manuscript was accepted by Phys. Fluids. Click here to see the version of record.

APPENDIX A: EXPERIMENTAL COMPONENTS AND MEASUREMENT SYSTEM

A. Full-field view method for interface tracking

We used the full-field view (FFV) photographic method to capture the kinematics of interface motion on a charge-coupled device (CCD) sensor whose output is recorded in real time on a video recorder for the experimental set-up in Fig. 13. The basic operation consisted of removing the divider to establish the initial condition necessary to follow the Lagrangian history of interface motion and measure its length stretch $\mathcal{L}(t)$. A uniform background light source is created using a 12 inch diameter integrating sphere, Lab sphere model US-120, which is positioned approximately one inch from the back of the cavity test cell. The sphere collects radiation from an internal source, Oriel light source attached to a PhotoMax illuminator powered by HP 6030 power supply, and integrates that radiation to create a uniform field of light within the sphere. The sphere exit port serves as a source of radiation that is diffusively emitted from the exit plane; luminance across the plane of the exit port is uniform and nearly Lambertian. The motion of the interface is captured by a Sony color video camera (DXC-950 3-CCD) and recorded on a Panasonic AG-6040 time-lapse video recorder for off-line processing. The camera produces high-quality images due to its ½ inch three-chip power hole-accumulated diode CCD which contains approximately 380,000 (768 (horizontal) × 494 (vertical)) effective pixels. The FFV method provides a global view of the interface structure.

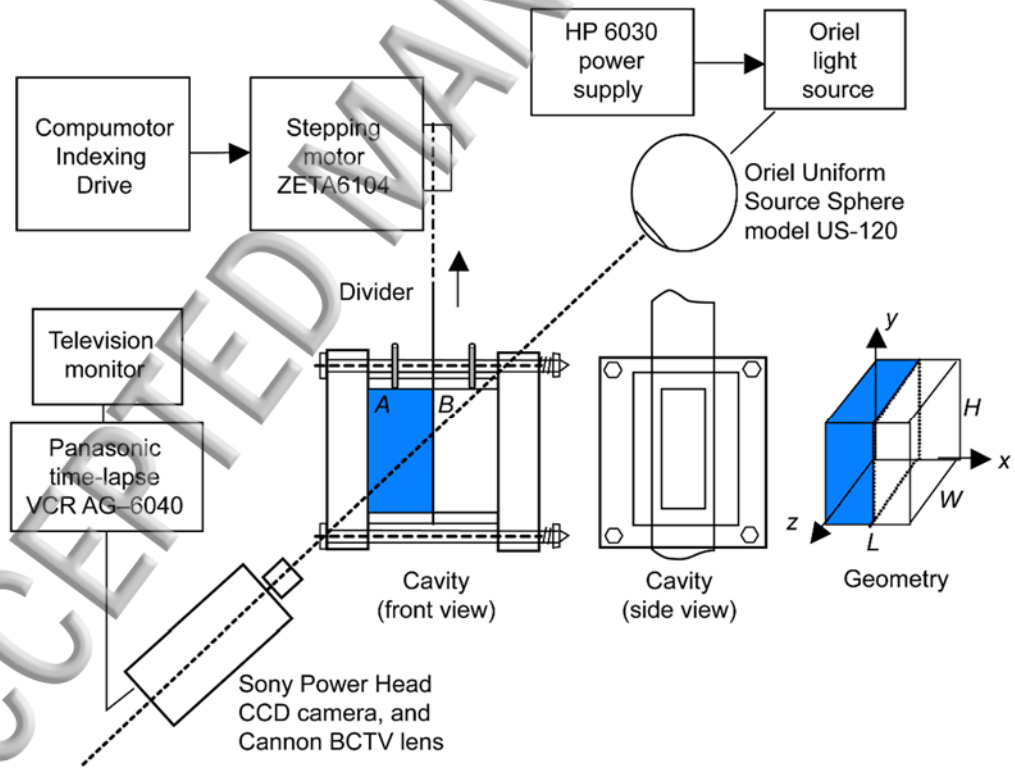

FIG 13. Experimental set-up (not to scale) to quantify interface motion using full-field view (FFV) method; for the planar laser-induced fluorescence (PLIF) method detailed in Part 2, we used a planar laser sheet in place of the Oriel light source; (VCR, videocassette recorder; CCD, charge-coupled device; BCTV, broadcast television).

This manuscript was accepted by Phys. Fluids. Click here to see the version of record.

B. Light source using planar laser sheet

We used a Gemini-PIV (200MJ, 30 Hz) Nd:YAG pulsed laser for planar laser-induced fluorescence (PLIF) measurements of the interface structure, detailed in Part 2, in place of the Oriel light source. The low concentration of rhodamine 6G dye used in the left chamber of the cavity in Fig. 13 acted as a conserved passive scalar which yielded the instantaneous interface structure similar to the works in Refs. (62,74). The measured molecular diffusivity of rhodamine 6G dye in water has been reported in Ref. 75 with a value of $D=3.0\times10^{-6}\,cm^2/s$ and yields a Schmidt number Sc = 3333 for $\bar{\nu}=0.01cm^2/s$ as shown in Table I below for cases (1-6).

1. Cavity test cell and mechanism

The initial configuration of two liquids (A, B) inside a cavity separated by a divider prior to establishing the initial condition from removal of the divider, is shown in Fig. 13. The motion of the divider is controlled by specifying a desired motion trajectory on the Compumotor indexing drive (Parker Compumotor SX6 system) that is communicated to the stepping motor (ZETA6104 model); the motion trajectory allows approximation of a pulse function as shown by Eq. (1).

The cavity consists of an enclosure with height H, width L, and depth W with respective dimensions of 5cm, 5cm and the following range: 0.2, 0.5, 1.0, 1.5, 2.0, 2.5, and 5.0 cm of depths as shown in Fig. 13 which allows experimental simulation from approximate two-dimensional Hele-Shaw cell to a three-dimensional configuration with aspect ratios Ar of: 0.04, 0.1, 0.2, 0.3, 0.4, 0.5, and 1.0. The enclosure is made from transparent acrylic material to allow for visualization of interface kinematics. The liquids are introduced inside the two chambers through capillary steel tubes at the top of the cavity using a syringe with a hypodermic needle; precautionary measures are taken to remove gas bubbles due to air entrapment. The enclosure consists of two sections, 2.5 cm each, separated by a thin polyethylene divider of thickness 0.01 cm. The two compartments are sealed by keeping the cavity test cell under compression using adjustable spring loaded clamps at the four corners of the cavity, and by using a thin film of vacuum grease between the two compartments; the vacuum grease is effective for sealing the compartments against leakage as well as to reduce friction when the divider is removed.

C. Image processing technique

Post-processing of the video recordings using image processing techniques common to the full-field view (FFV) and planar laser-induced fluorescence (PLIF) methods are described below.

1. Measurement of normalized concentration level of the interface

The normalized concentration level curves of the interface are determined as a function of intensity for a given image from calibration of concentration as a function of image intensity shown in Fig. 14(a). The image intensity is based on gray levels which span 0 to 255 representing respectively a black to white background image. The normalized concentration profile of the interface C calibrated as a function of intensity I is shown in Fig. 14(a), in which the measured average intensity of the interface corresponds to $\bar{I}_i$ with initial ($\bar{I}_{\min}$, $\bar{I}_{\max}$) and final $\bar{I}_f$ value

This manuscript was accepted by Phys. Fluids. Click here to see the version of record.

for the stably stratified configuration. The intensity profile at $y = H/2$ for the initial configuration is shown in Fig. 14(b); the intensity jump at $x = 2.5$ cm corresponds to the interface region, since the water and deuterium oxide and dye solution C_A, has a greater absorbance for incident photons, its intensity is lower compared to the water and deuterium oxide solution C_B, on the right hand side.

For the background image acquired at time zero, the average intensity profile for the left and the right side of the image ($\bar{I}_{\min}$, $\bar{I}_{\max}$) corresponding respectively to the initial normalized concentrations, C_A and C_B, on the left and right hand side of the cavity is shown in Fig. 14(b); $\bar{I}_i = (\bar{I}_{\max} + \bar{I}_{\min})/2$ gives the value of the intensity corresponding to the average concentration $\bar{C}$ of the interface initially at $x=L/2$. The final average intensity of the homogeneous region $\bar{I}_f$ is measured for a special case of the final configuration when the two fluids become homogenous over a long time scale. Figure 14(a) shows, from the measured intensities ($\bar{I}_{\min}$, $\bar{I}_{\max}$, $\bar{I}_i$ and $\bar{I}_f$), that the normalized concentration varies linearly with intensity which provides a means to determine the concentration

$$C = \left| \frac{\bar{I} - \bar{I}_{\max}}{\bar{I}_{\min} - \bar{I}_{\max}} \right| \qquad \text{(A1)}$$

band $0.0 \le C \le 1.0$ as a function of intensity, which is also used for measurement of the interface length stretch $\mathcal{L}(t) \equiv \bar{C}(t)$, its width $\delta w(t)$, and height $y(t)$.

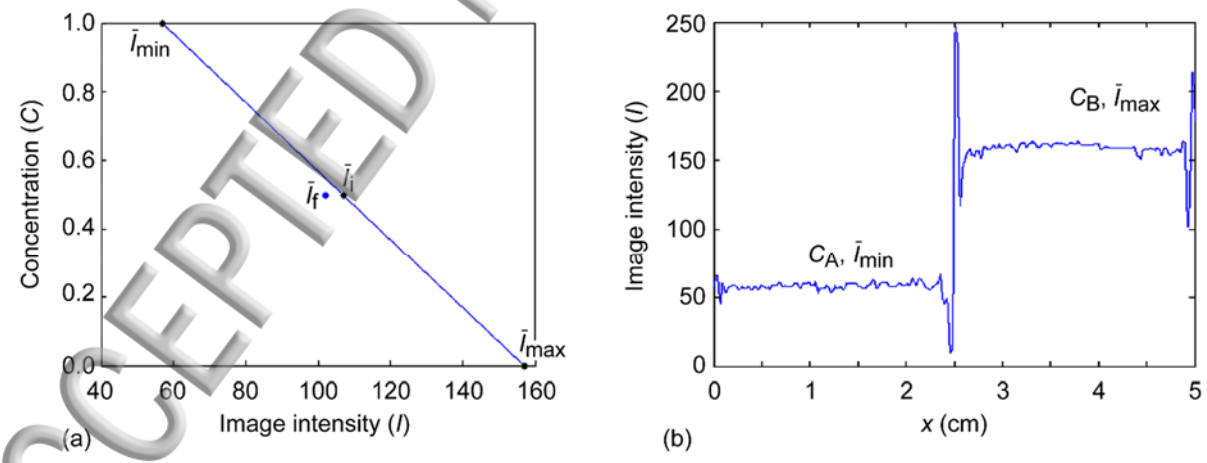

FIG. 14. Calibration of concentration as a function of image intensity measurements showing (a) normalized concentration C as a function of intensity I; (b) intensity profile at $y = H/2$ for the initial configuration of the interface.

2. Measurement of interface metrics

To quantify the kinematics of interface motion, we used Matlab to determine the metrics of the interface such as, length stretch $\mathcal{L}$(t), interface width $\delta w(t)$, and height $y(t)$; we also used the photo-editing programs in CorelPhoto-paint to operate on bitmap images and the image trace contour to operate on fuzzy regions. Quantification of the images is processed using image enhancement operations in MATLAB such as image trace contour, edge detection, and image histogram, and special functions to provide Euclidean distance between a set of pixels. Since the length stretch $\mathcal{L}$(t) of the interface is proportional to the number of pixels, its measurement is determined by summing the number of pixels of the interface. Similarly the interface width $\delta w(t)$ during mixing and height $y(t)$ after final stratification are measured.

D. Parametric range of experiments

To investigate buoyancy-driven mixing, we used a range of dilute mixtures of de-ionized water (H_2O) and deuterium oxide (D_2O), as well as mixtures of 1,2propylene-glycol (Pp.) and ethylene-glycol (Et.) with water which contained a volume fraction in the range of 2% to 22%, as shown in Table I. We consider liquid pairs to simulate both zero and finite jump in viscosity; the nearly zero jump in viscosity was obtained using dilute mixtures of the solute D_2O and solvent H_2O which contained volume fraction on the order of 2% with a methylene blue dye of very low concentration. Whereas, mixtures of ethylene and propylene-glycol with de-ionized water resulted in finite viscosity jumps. For color contrast we used either methylene blue dye or rhodamine 6G dye for fluid A, and kept fluid B clear.

The specific gravity was measured for the fluid pairs using calibrated hydrometers (Chase Instruments) with various range in specific gravity; for dilute mixtures of water with deuterium oxide we used a hydrometer with specific gravity range from 0.9950 to 1.0110 which has a precision error within ± 0.00005, whereas for alcohol mixtures the range runs from 1.000 to 1.070, with a precision error of ± 0.00025. The density can be calculated from the specific gravity using $s = \rho/\rho_w$, where $\Delta s/\bar{s} = \Delta\rho/\bar{\rho}$ in which $\bar{s}$ and $\bar{\rho}$ are average values. The reference values for the density of water ρ_w ($\rho_w = 0.997040\, gm/cm^3$ at 25^{0}C) and kinematic viscosity of various mixtures[76] were taken at ambient laboratory condition. The dye concentration is kept the same for all fluid pairs; the contrast between the blue and clear region facilitated tracking of the interface. The diffusion coefficient for methylene blue dye and water has been reported in Refs. 5 to have a value of $D = 3.0\times10^{-6} cm^2/s$ which is equivalent to the rhodamine 6G dye in water reported in Ref. 75 and implies equivalent Schmidt number Sc = 3333 for both systems, since the viscosities are also equal for cases (1-6) in Table I; whereas, the diffusion coefficients of alcohols with water have been reported in Refs. 76.

Table I shows the range of parameters and thermophysical property values for viscous liquid pairs. The limiting condition $\Delta\rho/\bar{\rho}=0$ for case 0 allows the testing of simulated microgravity condition. We use small amounts of D_2O in H_2O to adjust S_A and S_B for cases 1-6, this allows the attainment of the low values of density jump across the liquid interface. The kinematic viscosity values in cases 7-12 assume ideal mixtures that have linear variation in viscosity from the reference value. The jump in density varies within the range $5\times10^{-5}\le\Delta\rho/\bar{\rho}\le5.19\times10^{-2}$ and viscosity jump range of $0.00\le\Delta\nu/\bar{\nu}\le1.77$; in analogy to the Atwood number based on density $At=1/2(\Delta\rho/\bar{\rho})$, one based on viscosity may be expressed as $At_v=1/2(\Delta\nu/\bar{\nu})$. The low jump in density implies that the liquid pairs are well approximated as Boussinesq fluids, the jump in viscosity serves as a damping parameter. Even though cases 7 and 11 are identical in density jump, $\Delta\rho/\bar{\rho}=0.02817$, there is a substantial difference in viscosity jump $\Delta\nu/\bar{\nu}$, which is reflected in the decrease in Grashof number due to damping caused by the viscous force. Given the precision of our hydrometer the reliable limit of $\Delta s/\bar{s}$ is 0.00005 as shown for case 1, this implies a low limit of $Gr=6.13\times10^4$ for liquids with nearly zero jump in viscosity, however for alcohol mixtures it is possible to reach lower limits due to the larger viscosity values.

TABLE I. Parametric range of experiments.

Case	Fluids A/B	S_A	S_B	ν_A cm^2/s	ν_B cm^2/s	$\frac{\Delta\rho}{\bar{\rho}}=2At$	$\frac{\Delta\nu}{\bar{\nu}}$	Gr	Sc
0	H_2O+Dye+D_2O / H_2O+D_2O	1.0023	1.0023	0.01	0.01	0	0	0	---
1	H_2O+Dye+D_2O / H_2O+D_2O	0.9993	0.99925	0.01	0.01	0.00005	0.00	6.13×10^4	3333
2	H_2O+Dye+D_2O /H_2O+D_2O	0.99965	0.9994	0.01	0.01	0.00025	0.00	3.06×10^5	3333
3[a]	H_2O+Dye+D_2O /H_2O+D_2O	1.0000	0.9997	0.01	0.01	0.0003	0.00	3.7×10^5	3333
4[a,b]	H_2O+Dye+D_2O /H_2O+D_2O	1.0023	0.9997	0.01	0.01	0.00259	0.00	3.18×10^6	3333
5[a,b]	H_2O+Dye+D_2O /H_2O+D_2O	1.022	0.9998	0.01	0.01	0.02196	0.00	2.69×10^7	3333
6	H_2O+Dye+D_2O /H_2O+D_2O	1.0525	0.99925	0.01	0.01	0.05191	0.00	6.36×10^7	3333
7[b]	Et.+H_2O+ Dye /H_2O	1.026	0.9975	0.01158	0.01	0.02817	0.14643	2.96×10^7	1079
8	Et.+H_2O+Dye /H_2O	1.0505	0.9975	0.01316	0.01	0.05176	0.27288	4.73×10^7	1158
9	Pp.+H_2O+ Dye /H_2O	1.013	0.9975	0.08598	0.01	0.01542	1.58325	8.20×10^5	4799
10	Et.+H_2O+Dye /Pp.+ H_2O	1.026	1.013	0.01158	0.08598	0.01275	1.52522	6.56×10^5	4878
11	Pp.+H_2O+Dye /H_2O	1.026	0.9975	0.16196	0.01	0.02817	1.76739	4.67×10^5	8598
12	Et.+H_2O+Dye /Pp.+ H_2O	1.026	1.0135	0.01158	0.08598	0.01226	1.52522	6.31×10^5	4878

[a]The complete range of aspect ratios were addressed for these cases; the Peclet number is given by $Pe=GrSc$.
[b]Experiments also conducted in a microgravity (10^{-6} g_o) environment Ref. 45 for aspect ratio $Ar=0.2$; 1,2propylene glycol (Pp.), ethylene glycol (Et.).

APPENDIX B: CHARACTERISTIC OF IMPULSIVE PERTURBATION OF DIVIDER MOTION

The relationship between the initial potential energy which drives the flow field and folds the interface, and the injected kinetic energy perturbation which determines the transition from asymmetric to nearly symmetric RTM structure is considered. We show that the injected kinetic energy due to divider motion depends on the approximation of the local velocity profile near the divider; in particular we consider the uniform and linear Couette flow velocity approximations. The impulsive velocity perturbation of divider motion is approximated as a start-up or time development Couette flow in which the transient leads asymptotically to the steady state linear velocity profile. We contrast the effect of divider motion for simulated microgravity ($10^{-6}g_o$) condition using $\Delta\rho = 0$ and ground-based ($1g_o$) applications using $\Delta\rho > 0$, and deduce various approximations for the characteristic velocity of the flow field from an energy balance model.

1. Uniform velocity approximation

The approach of the interface toward a symmetric structure, requires that kinetic energy be injected into the system given as,

$$KE = \frac{1}{2}\overline{\rho}\int_0^W\int_0^H\int_0^L \vec{V}\cdot\vec{V}(x,y,z,t)\,dxdydz \tag{B1}$$

which yields for plane average localized parallel flow where $\vec{V}$ (x,y,z,t) = v(x,t),

$$KE = \frac{1}{2}\overline{\rho}WH\int_0^L \mathrm{v}^2\,(x,t)dx \tag{B2}$$

The approximation v = U_o is first considered which corresponds to uniform flow due to divider motion, since it yields the maximum kinetic energy that can be injected into the flow field, thus provides an upper bound. The injected kinetic energy for the uniform velocity approximation yields,

$$KE_U = \frac{1}{2}\overline{\rho}\forall U_o^{\,2} \tag{B3}$$

in which the volume is $\forall = WHL$ and the subscript U denotes uniform; the corresponding initial potential energy of the system is given as,

$$PE_o = \frac{1}{2}\Delta\rho n g_o \forall H \tag{B4}$$

where $\Delta\rho = (\rho_A - \rho_B)$. The injected kinetic energy serves as a source of initial disturbance or perturbation to the system and can affect symmetry, whereas the initial potential energy PE_o generates the flow field that drives interface motion and cause folding. Because of the coupling between KE and PE_o, the problem may be also looked from the viewpoint of how the total initial energy of the system

$$E_{To} = KE + PE_o \tag{B5}$$

This manuscript was accepted by Phys. Fluids. Click here to see the version of record.

drives interface motion to generate folding and approach symmetry. For the ideal initial condition of zero perturbation or disturbance corresponding to $U_o = 0$ considered in the computational model[6], interface motion is driven by potential energy only which yields symmetric RTM structures. However, experimentally a finite U_o is required which necessitates the injection of kinetic energy in the system. This indicates that there is a delicate balance between the initial potential energy PE_o available for interface motion that yields interface folding and the injected kinetic energy KE that controls the approach to symmetry. If the injected kinetic energy becomes too large then the initial disturbance is superimposed on the entire time history of the transient mixing process.

The ideal condition of having the two non-homogeneous fluids in intimate contact at an interface, with the configuration shown in Fig. 2, is possible under microgravity condition ($ng_o = 10^{-6} g_o$) since mechanical equilibrium is achieved in this limit. This ideal condition has been achieved by removing the divider in a microgravity environment at a low impulsive pulling velocity U_o on the order of 0.2 cm/s[45]. Since the body force is miniscule, this implies that the total initial energy

$$E_{To} = \frac{1}{2} V [\bar{\rho} U_o^2 + n g_o H \Delta\rho] \tag{B6}$$

can become very small, since the buoyancy term is negligible and the inertia term can be made as small as possible. The advantage of a microgravity environment is that the impulsive pulling velocity can be infinitesimally small so as not to disturb the interface, whereas in ground-based laboratory condition the low velocity limit is not practical for our problem. In addition the microgravity condition serves as a model environment to test the classical Couette flow model in which the effect of buoyancy does not affect the boundary layer at the interface induced by divider motion. The ideal initial condition, in which the interface is stationary has been used to study the effect of vibrational disturbance on the stability of the interface between two miscible liquids under microgravity condition[45]. However, this precludes the study of mixing due to steady body force since the interface is stabilized in microgravity condition without the vibrational input.

2. Couette-Poiseuille flows induced by divider motion: microgravity application

The impulsive velocity of the divider motion introduces a boundary layer localized near the interface at short times on the order of τ. The effect of the removal of the divider on the injected kinetic energy is approximated by assuming a linear velocity input v(x,t) in Eq. (B2) which represents steady shear Couette flow for sustained motion of the divider, when buoyancy force is negligible as in a microgravity environment $ng_o \to 0$ or the case of homogeneous fluids $\Delta\rho = 0$; this approximation renders convective acceleration negligible due to negligible buoyancy force. Even though motion of the divider is not sustained experimentally, the steady Couette flow approximation yields insight into the asymptotic solution. In this regard, for the experimental configuration shown in Fig. 2, the steady state velocity profile may be obtained from a balance between the vertical pressure gradient and viscous force as shown by Eq. (5) ($\bar{\mu} d^2v/dx^2 = dp/dy$) for the domain $0 \le x \le L/2$ which satisfies the boundary condition that v = 0 at x = 0 and v = U_o at $x = L/2$ and yields the solution,

$$v(x) = 2U_o \frac{x}{L} + P^* U_o \frac{x}{2L}(1 - 2\frac{x}{L}) \tag{B7}$$

in which P^* is a dimensionless pressure gradient given as $P^* = (L^2 / 2\bar{\mu}U_o)/(-dp_m / dy)$ and $p_m = p + \rho g_o y$ is the total hydrostatic pressure which includes the gravity term. Equation (B7) shows that the general velocity profile of Couette-Poiseuille flows consists of a superposition between the linear first term Couette shear flow due to divider motion and a parabolic second term or Poiseuille flow due to the pressure gradient. The deviation of the velocity profile from its linearity ($P^* = 0$) depends on the sign and magnitude of the dimensionless pressure gradient P^*; for $P^* > 0/P^* < 0$, pressure decreases/increases in the direction of flow. The velocity profile in Eq. (B7) is positive over the width of the cavity for $P^* > 0$; whereas for $P^* < 0$, the velocity profile can become negative over a portion of the cavity in which backflow may occur near the wall at rest.

The kinetic energy for the asymptotic solution may be approximated from the linear velocity distribution from the center plane $x = L/2$ of the divider to the left $x = 0$ and right $x = L$ walls, with corresponding boundary conditions v(0) = 0, v(L) = 0 and interior condition v($L/2$) = U_o; assuming that the pressure gradient is negligible. The linear velocity profile,

$$v(x) = \begin{cases} \dfrac{2U_0}{L} x & 0 \le x \le L/2 \\ \dfrac{2U_0}{L}(L - x) & L/2 \le x \le L \end{cases} \tag{B8}$$

as implied from Eq. (B7) is used to integrate the kinetic energy equation of Eq. (B2) between the limit $0 \le x \le L$ or use of symmetry conditions for either of the half space $0 \le x \le L/2$ or $L/2 \le x \le L$ yields,

$$KE_L = \frac{1}{6}\bar{\rho}\forall U_o^2 \tag{B9}$$

in which the subscript L denotes a linear velocity profile. The kinetic energy injection into the flow for the asymptotic solution given by Eq. (B9) corresponds to the case of a homogeneous fluid $\Delta\rho = 0$, since the effect of buoyancy is absent and the flow field is initially quiescent. This limiting case which corresponds to Gr = 0, simulated microgravity condition, and to no change in potential energy ΔPE of the system provides a means to isolate the effect of divider motion. In this case there is no background flow, generated by a change in potential energy, superimposed on the flow field due to divider motion.

To model the impulsive velocity profile of divider motion, the initial disturbance may be approximated as a suddenly accelerated divider which moves parallel to the stationary flat wall at a distance $L/2$. This analogy corresponds to the problem of flow formation or start-up transient in Couette motion[77], for an infinite plate in the vertical direction: that is the problem of how the velocity profile varies with time tending asymptotically to a linear distribution as the divider in Fig. 2 is removed. The short time velocity profile due to divider motion which serves as a model

This manuscript was accepted by Phys. Fluids. Click here to see the version of record.

of the impulsive velocity perturbation may be obtained from the approximate one-dimensional Navier-Stokes equation of Eq. (5),

$$\frac{\partial \mathrm{v}}{\partial t} = \bar{\nu}\frac{\partial^2 \mathrm{v}}{\partial x^2} \tag{B10}$$

with the initial condition: $t \le 0$, $v(x,0) = 0$ for all x, and boundary conditions for $t > 0$, $v(L/2,t) = U_o$ and $v(L,t) = 0$ for the right wall. Even though the condition at the centerline implies a step change in velocity for all time, the effect of an impulse for a short time scale can be derived from a step solution using superposition. The pressure can only be a function of time for this flow; hence it is absorbed into the velocity by a change in variable: that is, $\mathrm{v} = \mathrm{v}' + \int (1/\bar{\rho})(dp/dy)dt$. For the domain, $L/2 \le x \le L$, a similarity solution[77] can be obtained in the form of a series of complementary error function given as

$$\begin{aligned}\frac{\mathrm{v}}{\mathrm{U}_o} &= \sum_{n=0}^{\infty} erfc(2n\eta_1 + \eta) - \sum_{n=0}^{\infty} erfc(2(n+1)\eta_1 - \eta) \\ &= erfc\eta - erfc(2\eta_1 - \eta) + erfc(2\eta_1 + \eta) - erfc(4\eta_1 - \eta) + erfc(4\eta_1 + \eta) - \ldots + \ldots\end{aligned} \tag{B11}$$

where $\eta = (x - L/2)/2\sqrt{\bar{\nu}t}$ and $\eta_1 = L/4\sqrt{\bar{\nu}t}$. The boundary layer thickness δ, measured relative to divider motion at $x = L/2$, may be approximated to lie between the values for which $v/U_o = 0.01$, $\eta = 2.0$ and $v/U_o = 0.48$, $\eta = 0.5$; the boundary layer thickness is defined as the distance from the centerline at $x = L/2$ for which $v/U_o = 0.1$. The approximate value of the boundary layer thickness for both sides of the interface $\delta_b = 2\delta$ becomes,

$$\delta_b = 4.6\sqrt{\bar{\nu}H/U_o} \tag{B12}$$

The long time solution for the velocity distribution for $L/2 \le x \le L$ which gives insight into the functional form of the velocity perturbation can be obtained alternatively in terms of a Fourier series[76] as

$$\frac{\mathrm{v}}{U_o} = 2(1 - \frac{x}{L}) - \frac{2}{\pi}\sum_{n=1}^{\infty}\frac{1}{n}\exp(-\frac{4n^2\pi^2\bar{\nu}^2}{L^2}t)\sin\frac{2n\pi x}{L} \tag{B13}$$

This form of the solution shows that the asymptotic value of the Fourier series vanishes exponentially as $t \to \infty$; the linear Couette flow solution is approached in this limit. For impulsively accelerated flow, the impulsive kinetic energy equation,

$$KE_i = \frac{1}{2}\bar{\rho}WH\int_{L/2-\delta}^{L/2+\delta} \mathrm{v}^2(x,t)dx \tag{B14}$$

may be integrated within the boundary layer, by approximating the velocity profile to be similar to the linear case of Eq. (B8) with the inclusion of the boundary layer thickness,

$v(x) = (2U_0/L)(x - L/2 + \delta)$, $0 \le x \le L/2$, and $v(x) = (2U_0/L)(L/2 + \delta - x)$ for $L/2 \le x \le L$, and shifting the coordinate to *L/2*. The impulsive kinetic energy injected becomes,

$$KE_i = \frac{4}{3}\bar{\rho}\forall U_o^2\left(\frac{\delta}{L}\right)^3 \tag{B15}$$

in which subscript *i* denotes impulsive. The impulsive injected kinetic energy KE_i is equal to the asymptotic KE_L of Eq. (B9) for Couette flow when the boundary layer extends to the wall $\delta = L/2$. Whereas, the injected kinetic energy for the linear velocity profile $KE_L = 1/3KE_U$ is one-third that of the uniform velocity profile of Eq. (B3) which indicates that the uniform profile serves as a maximum bound.

The first order approximation of the velocity profile yields a cubic dependence of the boundary layer thickness on KE_i which predicts the minimum bound of KE_i because the inertia term becomes small. However, an impulsive uniform velocity approximation can be used in Eq. (B14) to find the maximum bound of injected kinetic energy KE, which yields

$$KE_{i_U} = \bar{\rho}\forall U_o^2\left(\frac{\delta}{L}\right) \tag{B16}$$

In between the two limits, that bounds the minimum KE_i of Eq. (B15) for which the inertia term is small and maximum KE_{i_U} given by Eq. (B16) for which the inertia term can become on the same order as the buoyancy term, higher order approximations of the velocity profile can lead to a range of possible values for KE_i.

3. Characteristic velocity scales

For short characteristic time, an energy balance model for a frictionless conservative system can lead to useful estimate of the characteristic velocity U_C. From an energy balance, it can be shown that the kinetic energy $(1/2\bar{\rho}\forall U_c^2)$ over a short time interval is equal to the difference in potential energy between the initial and final state $(\Delta PE_{max} = (\forall/4)Hng_o\Delta\rho = (1/2)PE_o)$ plus injected kinetic energy into the system. The approximate forms of the velocity profile in the neighborhood of the divider namely—uniform, linear, and their impulsive approximations—yield the following expressions for the characteristic velocity from the energy balance model,

$$U_{CU} = \sqrt{U_o^2 + ng_oHA_t} \tag{B17}$$

$$U_{CL} = \sqrt{\frac{U_o^2}{3} + ng_oHA_t} \tag{B18}$$

This manuscript was accepted by Phys. Fluids. Click here to see the version of record.

$$U_{Ci_L} = \sqrt{\frac{8U_o^2}{3}\left(\frac{\delta}{L}\right)^3 + ng_o HA_t} \tag{B19}$$

$$U_{Ci_U} = \sqrt{2U_o^2\frac{\delta}{L} + ng_o HA_t} \tag{B20}$$

in which $\delta = 2.3\sqrt{\nu\tau}$ and the Atwood number $At = \Delta\rho / 2\bar{\rho} = (\rho_A - \rho_B)/(\rho_A + \rho_B)$; the expression for the boundary layer thickness near the interface is expressed as a function of τ to emphasize its dependence on pulse duration $\tau = H/U_o$. The characteristic velocity is a function of the inertia terms that represent injected kinetic energy due to divider motion and the buoyancy terms that represent initial potential energy of the system per unit mass $PE_o/\bar{\rho}\forall$. For a short duration pulse $\tau \to 0$ that generates a boundary layer flow the potential energy can be dominant over the kinetic energy input, whereas for a long pulse duration $\tau \to \infty$ in which $\delta = L/2$ Eqs. (B19, B20) reduce respectively to Eqs. (B18), (B17) which correspond to the approximation of linear velocity Couette flow and constant velocity uniform flow.

TABLE II. The initial potential energy PE_o and injected kinetic energy KE and corresponding characteristic velocity U_c of flow field contrasting ground-based $Gr = 3.18\times10^6$ or $Pe = 1.06\times10^{10}$ and simulated microgravity conditions ($Gr = 0$) for $Ar = 0.2$.

U_o cm/s	Re_i	PE_o erg	KE_L erg	KE_{iL}/KE_{iU} erg / erg	KE_U erg	U_{CL} cm/s	U_{GL}/U_{GU} cm/s /cm/s	U_{CU} cm/s
$Gr = 3.18\times10^6$ or $Pe = 1.06\times10^{10}$								
0	0	159.3	0	0/0	0	2.52	2.52/2.52	2.52
3	1500	159.3	37.5	0.06/13.3	112.5	3.06	2.52/2.72	3.92
5	2500	159.3	104.2	0.08/28.7	312.5	3.83	2.52/2.94	5.60
7	3500	159.3	204.2	0.09/47.4	612.5	4.76	2.52/3.19	7.44
10	5000	159.3	415.9	0.11/79.8	1247.6	6.29	2.52/3.57	10.31
20	10000	159.3	1663.4	0.16/229.5	4990.2	11.82	2.52/4.97	20.16
40	20000	159.3	6653.6	0.22/638.7	19960.7	23.23	2.52/7.64	40.08
$Gr = 0$								
5	2500	0	104.1	0.08/28.7	312.3	2.90	0.081/1.52	5.0

The long duration pulse $\tau = H/U_o$ is of practical relevance to microgravity experiments in which the divider can be pulled infinitely slow to achieve mechanical equilibrium between two non-homogeneous fluids. For fast divider pulling or large impulsive velocity in a microgravity environment, the inertia term in Eqs. (B17-B20) becomes dominant over the buoyancy term. The predicted magnitude of the characteristic velocities from Eqs. (B17-B20) are shown in Table II as

This manuscript was accepted by Phys. Fluids. Click here to see the version of record.

well as the corresponding initial potential energy Eq. (B4) and kinetic energies—Eq. (B3) uniform, Eq. (B9) linear, and Eqs. (B15,B16) impulsive—for a range of impulsive Reynolds numbers Re_i. The Grashof numbers $Gr = 0$ and $Gr = 3.18\times10^6$ correspond respectively to cases 0 and 4 in Table I for aspect ratio Ar = 0.2. Relative to the initial potential energy PE_o = 159.3 ergs for $Gr = 3.18\times10^6$ at $Ar = 0.2$, the potential energy for $Gr = 3.73\times10^5$ is PE_o = 18.3 ergs for Ar = 0.2 and PE_o = 27.5 ergs for $Ar = 0.3$, whereas for $Gr = 2.69\times10^7$ there is a substantial increase in initial potential energy to PE_o = 1356.7 ergs with the large jump in density for Ar = 0.2. The usefulness of the characteristic velocity expressions Eqs. (B17-B20), assessed against experimental measurements of the magnitude of the velocity field in Part 2 shows reasonable approximation of the characteristic velocities from Eqs. (B17) and (B18) for a limited range of Re_i, while Eqs. (B19) and (B20) apply for the entire range of Re_i considered as shown in Table II.

APPENDIX C: DAMPED HARMONIC OSCILLATOR MODEL OF SLOSHING

The transient response characteristic of sloshing such as its damped natural frequency f_d is quantified experimentally from the time signal of the length stretch of the interface, and its undamped natural frequency f_n approximated using a second order model of a damped harmonic oscillator. This approximation applies since only the first mode of sloshing is observed for $Gr = 3.18\times10^6$ or $Pe = 1.06\times10^{10}$ analogous to a solid body of a mechanical system.

For the damped harmonic oscillator model of sloshing, the undamped natural frequency and damping ratio is estimated from the experimental data for the underdamped cases using the method of logarithmic decrement[79] ; the estimation of the logarithmic decrement δ_d from the time signal is given as

$$\delta_d = \frac{1}{n}\ln\left|\frac{\ell\%_{p_1}}{\ell\%_{p_{n+1}}}\right| \tag{C1}$$

in which $\ell\%_{p_1}$ and $\ell\%_{p_{n+1}}$ correspond to the maximum discrete amplitude of oscillations of the length stretch separated by n cycles as shown in Figs. 6(a,b). Sloshing is approximated as the long time response of the interface to initial input disturbance over the time scale T_f which leads to stable stratification.

The damped natural frequency f_d is estimated from the time signal of the length stretch of the interface from Figs. 6(a,b) by averaging over the representative time interval. The damping ratio ξ is calculated from

$$\xi = \frac{\delta_d}{\sqrt{4\pi^2 + \delta_d{}^2}} \tag{C2}$$

and the undamped natural frequency of the interface can be estimated from

This manuscript was accepted by Phys. Fluids. Click here to see the version of record.

$$\omega = \frac{\omega_d}{\sqrt{1-\xi^2}} \tag{C3}$$

in which $\omega_d = 2\pi f_d$. The experimentally calculated values of the damped natural frequency (f_d, ω_d), undamped natural frequency (f_n, ω_n), and damping ratio ξ can be used to compare with an approximate second-order model of a damped oscillator such as

$$\ddot{L} + 2\xi\omega_n \dot{L} + \omega_n^2 L = f(t) \tag{C4}$$

where $f(t)$ is the input that generates mixing, over the short time scale T_{SF} that includes the disturbance due to divider motion and the resulting stretching and folding of the interface, which sets-up the condition for self-induced sloshing; ω_n is the normalized undamped natural frequency of the system given by Eq. (27) in terms of system variables obtained from the standard form of Eq. (C4), and $L(t)$ is the length stretch ratio $l(t)/l_o$ with the property that at $t = 0$, $L(0) = 1$. We consider the initial condition response of Eq. (C4) to a step function input modeled with the condition that $L(t) = 0$ for $t < 0$ and $L(t) = 1$ for $t > 0$, and used the transient response as performance characteristics to predict the undamped natural frequency and damping ratio. For an underdamped system, $0 < \xi < 1$, the transient response from Eq. (C4) yields

$$L(t) = 1 - \frac{e^{-\xi\omega_n t}}{\sqrt{1-\xi^2}} \sin\left(\omega_d t + \tan^{-1}\frac{\sqrt{1-\xi^2}}{\xi}\right), \quad t \geq 0 \tag{C5}$$

The damping ratio ξ in Eq. (C5) can be estimated from the speed of decay of the transient response which corresponds to the settling time T_s of the system. The settling time T_s can be measured in terms of the time constant $T = 1/\xi\omega_n$ of the envelop curves; for a 2% tolerance band of the response, T_s is given as

$$T_s = \frac{4}{\xi\omega_n} \tag{C6}$$

Combining Eqs. (C3) and (C6) shows that the damping ratio ξ_m, subscript $_m$ denotes the second-order model, can be estimated from

$$\xi_m = \sqrt{\frac{16}{T_s^2\omega_d^2 + 16}} \tag{C7}$$

The damped frequency ω_d and the settling time T_s of the system, are obtained from the time signal and used to estimate the damping ratio ξ_m and undamped natural frequency ω_m of the second-order model. Table III shows a comparison between calculated values of the undamped natural frequency and damping ratio from the experimental time signal to the prediction of the second-order model Eq. (C4), and the inviscid theory of oscillation of two superposed fluids for a sharp δ_0 and diffused δ_D interface. The results from the second-order model show that as the aspect ratio of the cavity increases the model compares favorably to the experimental measurements as well as the inviscid theory of oscillation of two superposed fluids for 2D approximation.

TABLE III. Comparison of undamped natural frequency to prediction from harmonic oscillator model, denoted by subscript *m*, of interface sloshing and the inviscid theory of two superposed fluids for sharp δ_0 and diffused δ_D interface for a range of aspect ratios and fixed $Gr=3.18\times10^6$ or $Pe=1.06\times10^{10}$.

Ar	ω *rad/s*	ξ	ω_m *rad/s*	ξ_m	δ_0 *rad/s*	δ_D *rad/s*
0.04	0.023	0.8	0.036	0.922	-----	-----
0.10	0.612	0.561	0.539	0.339	-----	-----
0.20	0.696	0.280	0.693	0.266	0.856	0.716
0.50	0.649	0.198	0.653	0.226	-----	-----
1.0	0.619	0.174	0.621	0.195	-----	-----

The disparity between model and experiment of the undamped natural frequency for Ar ≤ 0.1 is attributed to the low number of oscillations from the time signal. The model is expected to hold for 2D flows which are bounded by the neighborhood of Ar ≈ 0.2; however for Ar ≥ 0.5, though the flow field is expected to transition to 3D, the model predicts relatively well. The closest matching condition between model and experiment occurs at *Ar = 0.2*; the prediction of the model ($\omega_m = 0.693 rad/s$, $\xi_m = 0.266$) shows reasonable agreement to the experimental measurements ($\omega = 0.696\ rad/s$, $\xi = 0.280$) and, the approximated undamped natural frequency $\omega_n = 0.712 rad/s$ given by Eq. (27) from scaling and, the inviscid theory of oscillation of two superposed fluids for a diffused interface δ_D for this approximate 2D cavity. The decrease in damping ratio from $\xi = 0.8$ for *Ar = 0.04* to $\xi = 0.174$ for *Ar = 1.0* as the aspect ratio increase indicates a decrease in viscous effects owing to the close proximity of the walls for small aspect ratios, hence the system response becomes less sluggish. In contrast to the approximate damped oscillator model of Eq. (C4) for single mode, a more general model of a damped parametric harmonic oscillator for higher mode numbers based on linearized quasipotential equations, that describes the displacement of the interface between two fluids in which one has a density much smaller than the other $\rho_B \ll \rho_A$, has been described in Ref. 80 for the underdamped limit.

[1]D.J. Gerbi, W.C. Egber, D.A. Ender, P.C.W. Leung, K.B. Rochford, J.W. Virde, E.L. Cook, "Growth of organic crystals in a microgravity environment," J. Crystal Growth, **76**, 673-680 (1986).

[2]J.D. Alexander, S. Amiroudine, J. Ouazzani, F. Rosenberger, "Analysis of the low gravity tolerance of Bridgman-Stockbarger crystal growth, II. Transient and periodic accelerations," J. Crystal Growth, **113**, 21-38 (1991).
[3]W.M.B. Duval, N.B. Singh, M.E. Glicksman, "Physical vapor transport of mercurous chloride crystals: Design of a microgravity experiment," J. Crystal Growth, **174,** 120-129 (1997).
[4]M.D. Radcliffe, J.E. Steffer, E.L. Cook, J.F. Cotting, C.R. Miller, M.C. Drake, F.S. Schroeder, and D. Jr. Stevens, "Organic crystals in low Earth orbit," J. Crystal Growth, **92,** 581-590 (1988).
[5]G.D. Roberts, J.K. Sutter, R. Balasubramaniam, W.K. Fowlis, M.D. Radcliffe, M.C. Drake, "Simulation of fluid flows during growth of organic crystals in microgravity," NASA TM 88921, Lewis Research Center (1987); D.G. Leaist, "The effects of aggregation, counterion binding, and added NaCl on diffusion of aqueous methylene blue," Can. J. Chem., **66,** 2452-2457 (1988); K.L. Kosta, M. D. Radcliffe, and E. von Meerwall, "Diffusion coefficients of methylene blue and thioflavin T dyes in methanol solution," J. Phys. Chem., **96**, 2289-2292 (1992).
[6] W.M.B. Duval, "Flow field topology of transient mixing driven by buoyancy," Chaos **14**, (3), 716-738 (2004).
[7]J.G. Franjione, W.K. Leong, J.M. Ottino, "Symmetries within chaos: A route to effective mixing," Phys. of Fluids, A **1** (11), 1772-1783 (1989).
[8] M. Chate, E. Villermaux, J.M. Chomaz, *Mixing Chaos and Turbulence* (Kluwer Academic / Plenum Publishers, 1996), 1-8.
[9] L.H. Kellog, C.A. Stewart, "Mixing by chaotic advection in an infinite Prandtl number fluid and implications for mantle convection," Phys. Fluids, A **3** (5), 1374-1378 (1991).
[10] D.V. Khakhar, H. Rising, J.M. Ottino, "An analysis of chaotic mixing in two chaotic flows," J. Fluid Mech., **172**, 355-377 (1986).
[11]H. Aref, S. Balanchandar, "Chaotic advection in a Stokes flow," Phys. Fluids, **29**(11), 3515-3521 (1986).
[12] J. Chaiken, R. Chevray, M. Tabor, Q.M. Tan, "Experimental study of Lagrangian turbulence in a Stokes' flow," Proc. R. Soc. London A, **408**, 165-174 (1986).
[13]C.W. Leong , J.M. Ottino, "Experiments on mixing due to chaotic advection in a cavity," J. Fluid. Mech., **209**, 463-499 (1989).
[14]M. Liu, R.L. Peskin, F.J. Muzzio, C.W. Leong, "Structure of the stretching field in chaotic cavity flows,"AIChE Journal, **40,** (8), 1273-1286 (1994).
[15]G.L. Brown, and A. Roshko, "On density effects and large scale structures in turbulent mixing layers," J. Fluid Mech. **64** (4), 775-816 (1974).
[16] R.D. Moser, and M.M. Rogers, "Mixing transition and the cascade to small scales in a plane mixing layer," Phys. of Fluids A **31**(5), 1128-1134 (1991).
[17] W.R. Hawthorne, D.S. Wendell, H.C. Hottel, "Mixing and Combustion in Turbulent Gas Jets," In Third Symposium on Combustion and Flame Explosion Phenomena, Baltimore, Williams& Wilking, 266-288, (1949).
[18]A.D. Mc Ewan, "The kinematics of stratified mixing through internal wavebreaking," J. Fluid Mech., **128**, 47-57 (1983a).
[19] A.D. Mc Ewan, "Internal mixing in stratified fluids," J. Fluid Mech., **128**, 59-80 (1983b).
[20] M.G. Brown, K.B. Smith, "Ocean stirring and chaotic low-order dynamics," Phys. of Fluids A, **3** (5), 1186-1192 (1991).
[21]Y. Noh, I.S. Kang, "Large eddy simulation of particle settling in the ocean mixed layer," Phys. of Fluids, **18**, 085109-1-15 (2006).

[22]G. Aharon, V. Rom-Kedar, H. Gildor, "When complexity leads to simplicity: Ocean surface mixing simplified by vertical convection," Phys. of Fluids, **24**, 056603-1-13 (2006).
[23]G. Haller, D. Yuan, "Lagrangian coherent structures and mixing in two-dimensional turbulence," Physica, D, **147**, 352-370 (2000).
[24] G. Haller, "Lagrangian coherent structures from approximate velocity data," Phys. of Fluids, **14**, (6), 1851-1861 (2002).
[25]J. Hardenberg, K. Fraedrich, F. Lunkeit, A. Provenzale, "Transient chaotic mixing during a baroclinic life cycle," Chaos, **10**(1), 122-134 (2000).
[26] W.M.B. Duval, D.A. Jacqmin, "Interfacial dynamics of two liquids under an oscillating gravitational field," AIAA Journal, **28(**11), 1933-1941 (1990); D. A. Jacqmin., W.M.B. Duval, "Small scale instabilities caused by oscillations normal to a viscous fluid-fluid interface," J. Fluid Mech. **196**, 495-511 (1988).
[27]W.M.B. Duval, "The kinematics of buoyancy induced mixing," European Symposium on Materials and Fluid Sciences in Microgravity, Universite Libre de Bruxelles, Belgium, 855-861 (1992).
[28]V.K. Siddavaram, and G.M. Homsy, "The effects of gravity modulation on fluid mixing. Part 1. Harmonic modulation," J. Fluid Mech. **562**, 445-475 (2006).
[29]J.R. Thomson, J. Casademunt, and J. Vinals, "Cavity flow induced by a fluctuating acceleration field," Phys. Fluids **7**, 292-301 (1995).
[30]V.K. Siddavaram, and G.M. Homsy, "The effects of gravity modulation on fluid mixing. Part 2. Stochastic modulation," J. Fluid Mech. **579**, 445-466 (2007).
[31]D.L. Youngs, "Three-dimensional numerical simulation of turbulent mixing by Rayleigh-Taylor instability," Phys. Fluids A **3**, 1312-1320 (1991).
[32]P.F. Linden, and J.M. Redondo, "Molecular mixing in Rayleigh-Taylor instability. Part I: Global mixing," Phys. Fluids A **3**, 1269-1277 (1991).
[33]P.F. Linden, J.M. Redondo, and D.L. Youngs, "Molecular mixing in Rayleigh-Taylor instability," J. Fluid Mech. **265**, 97-124 (1994).
[34]S.B. Dalziel, P.F. Linden, and D.L. Youngs, "Self-similarity and internal structure of turbulence induced by Rayleigh-Taylor instability," J. Fluid Mech. **399**, 1-48 (1999).
[35]J.M. Redondo, and G. Garzon, "Multifractal structure and intermittent mixing in Rayleigh-Taylor driven fronts," Proceedings of the 9th International Workshop on The Physics of Compressible Turbulent Mixing, July 2004.
[36] Q. Zhou, "Temporal evolution and scaling of mixing in two-dimensional Rayleigh-Taylor turbulence," Phys. Fluids **25**, 085107 (2013).
[37] B.-J. Gréa, "The rapid acceleration model and the growth rate of a turbulent mixing zone induced by Rayleigh-Taylor instability," Phys. Fluids **25**, 015118 (2013).
[38]J. M. Ottino, *The Kinematics of Mixing: stretching, chaos, and transport* (Cambridge University Press, 1989), 1-16, 117-125, 154-158.
[39]M.J. Andrews, D.B. Spalding, "A simple experiment to investigate two-dimensional mixing by Rayleigh-Taylor instability," Phys. Fluids A **2** (6), 922-927 (1990).
[40]P.F. Linden, and J.E. Simpson, "Gravity-driven flows in a turbulent fluid," J. Fluid Mech. **172**, 481-497 (1986).
[41]J.E. Simpson, and P.F. Linden, "Frontogenesis in a fluid with horizontal density gradients," J.

Fluid Mech. **202**, 1-16 (1989).
[42]D. Jacqmin, "Frontogenesis driven by horizontally quadratic distributions of density," J. Fluid Mech. **228**, 1-24 (1991).
[43]L. Lemaigre, M.A. Budroni, L.A. Riolfo, P. Grosfils, and A. De Wit, "Asymmetric Rayleigh-Taylor and double diffusive fingers in reactive systems," Phys. Fluids, **25**, 037112 (2012).
[44]M.A. Budroni, M. Rustici, E. Tiezzi, "On the origin of chaos in the Belousov-Zhabotinsky reaction in closed and unstirred reactors," Math. Modell. Nat. Phenom., **6**, 226-242 (2011).
[45]B.V. Tryggvason, R.F. Redden, R.A. Herring, W.M.B. Duval, R.W. Smith, K.S. Rezkallah, and S. Varma, " The vibration environment on the international space station: Its significance to fluid-based experiments," Acta Astronaut. **48**(2-3), 59-70 (2001).
[46]R.A. Wooding, " Instability of a viscous fluid of variable density in a vertical Hele-Shaw cell," J. Fluid Mech. **7**(4), 501-515 (1960).
[47]F. Haudin, L.A. Riolfo, B. Knaepen, G.M. Homsy, and A. De Wit, "Experimental study of a buoyancy-driven instability of a miscible horizontal displacement in a Hele-Shaw cell," Phys. of Fluids, **26**, 044102 (2014).
[48]P.S. Perera, R.F. Sekerka, "Nonsolenoidal flow in a liquid diffusion couple," Phys. Fluids **9** (2), 376-391 (1997).
[49]S. Chandrasekhar, *Hydrodynamic and Hydromagnetic Stability* (Oxford University Press, Oxford, UK, 1961), 441-447.
[50]C.E. Niederhaus and J.W. Jacobs, "Experimental study of the Richtmyer-Meshkov instability of incompressible fluids," J. Fluid Mech., **485**, 243-277 (2003); J. W. Jacobs and J.M. Sheeley, "Experimental study of incompressible Richtmyer-Meshkov instability," Phys. of Fluids, **8**, 405-415 (1996); R.D. Richtmyer, "Taylor instability in shock acceleration of compressible fluids," Commun. Pure Appl. Maths **13**, 297-319, (1960); E.E. Meshkov, "Instability of the interface of two gases accelerated by a shock wave," Izv. Akad. Nauk SSSR Mekh. Zhid. I Gaza **4**, 151-157 (1969).
[51]M. Ratafia, "Experimental investigation of Rayleigh-Taylor instability," Phys. Fluids, **16** (8), 1207-1210 (1975).
[52]D.Youngs, "Numerical simulation of turbulent mixing by Rayleigh-Taylor instability," Physica, **12**D, 32-44 (1984).
[53]G. Tryggvason, "Numerical simulations of the Rayleigh-Taylor instability," J. Comp. Phys., **75**, 253-282 (1988).
[54]J.T.Waddell, C.E. Niederhaus, and J.W. Jacobs, "Experimental study of Rayleigh-Taylor instability: Low Atwood number liquid systems with single-mode initial perturbations, " Phys. Fluids, **13** (5), 1263-1273 (2001).
[55]P. Ramaprabhu, G. Dimonte, P. Woodward, C. Fryer, G. Rockefeller, K. Muthuraman, P.-H. Lin, and J. Jayaraj, "The late-time dynamics of the single-mode Rayleigh-Taylor instability," Phys. Fluids **24**, 074107 (2012).
[56] J.S. Turner, *Buoyancy Effects in Fluids* (Cambridge University Press, Cambridge, MA.,1973), 94-102, 120-123.
[57]D.A. Birch and M.A. Sundermeyer, "Breaking internal wave groups: Mixing and momentum fluxes," Phys. Fluids **23**, 096602 (2011).

[58] M.V. Berry, N.L. Balazs, M. Tabor, and A. Voros, "Quantum Maps," Ann. Phys., **122**, 26-63, (1979).
[59] K.Y. Yang, Q. Zhang," Small amplitude theory of Richtmyer-Meshkov instability," Phys. Fluids, 6, 1856-1873 (1994); M. Koichi, "Exact solution to the general Riemann problem in nonuniform and nonstationary media: A simplified analysis of a shock wave accelerated at a constant rate," J. Math. Phys., **51**(12), 123102-123102-13 (2010).
[60] M. Brouillette, M. and B. Sturtevant, "Experiments on the Richtmyer-Meshkov instability: single-scale perturbations on a continuous interface", J. Fluid Mech, **263**, 271-292 (1994); C. Cavailler, P. Mercier, G. Rodriguez, and J. F. Haas, "A new vertical shock tube for Rayleigh-Taylor instability measurements". Proc. 17th ISSWST at Bethlehem PA, Current Topics in Shock Waves (ed. Y. Kim), **208**, 564-569 (1990); R. Bonazza and B. Sturtevant, "X-ray measurements of growth rates at a gas interface accelerated by shock waves", Phys. Fluids, **8**, 2496-2512, (1996).
[61] K. Balakrishnan, "Explosion-driven Rayleigh-Taylor instability in gas-particle mixtures," Phys. Fluids **26**, 0433303 (2014).
[62] P.E. Dimotakis, R.C. Miake-Lye, D.A. Papantoniou, " Structure and dynamics of round turbulent jets," Phys. Fluids **26**, 3185-3192 (1983).
[63] G.C. Orlicz, S. Balasubramaniam, P. Vorobieff, and K.P. Prestridge "Mixing transition in a shocked variable-density flow," Phys. Fluids **27**, 114102 (2015).
[64] S. Saeki, H. Madarame, K. Okamoto, "Self-induced sloshing excited by a horizontally injected plane jet," J. Fluid Mech., **448**, 81-114 (2001).
[65] A.A. Andronov, E. A. Vitt, and S.E. Khaiken, *Theory of Oscillators* (Oxford: Pergamon Press, 1966), 15-36.
[66] H. Lamb, *Hydrodynamics* (Cambridge University Press, 1932), 370-372.
[67] P.G. Drazin, W.H. Reid, *Hydrodynamic Stability* (Cambridge University Press, 1982), 324-325, 363.
[68] L. Rayleigh, " Investigation of the character of the equilibrium of an incompressible heavy fluid of variable density," Proc. London Math. Soc. **14**, 170-177 (1883).
[69] M. Golubitsky, D. Schaeffer, "A theory for imperfect bifurcation via singularity theory," *Comm. of Pure and App. Math.*, **32**, 21-98 (1979).
[70] C. Lanczos, *The Variational Principles of Mechanics* (Dover Publications, Inc., New York, 1970), 177-178.
[71] A.A. Kovitz, "Static fluid interfaces external to a right circular cylinder- experiment and theory," J. Colloid Interface Sci., **50,** 125-142 (1975); ibid. **52,** 412-413 (1975).
[72] M. Schroeder, *Fractals, Chaos, Power Laws* (W.H. Freeman and Company, New York, 1970) 103-119.
[73] M. Giona, S. Cerbelli, and A. Adrover, "Quantitative analysis of mixing structures in chaotic flows generated by infinitely fast reactions in the presence of diffusion," J. Phys. Chem. A, **106**, 5722-5736 (2002).
[74] M.M. Koochesfahani, and P.E. Dimotakis, "Laser-induced fluorescence measurements of mixed fluid concentration in a liquid plane shear layer," AIAA J. **23**, 1700-1707 (1985).
[75] E. L. Elson, and D. Magde , "Fluorescence correlation spectroscopy.I. Conceptual basis and theory, " Biopolymers, **13**, 1-27 (1974); D. Magde, E. L. Elson, and W. W. Webb, Fluorescence correlation spectroscopy II. An experimental realization,", ibid. **13**, 29-61 (1974); P. Gendron, F. Avaltroni and K.J. Wilkinson, "Diffusion coefficients of several rhodamine derivatives as

determined by pulsed field gradient-nuclear magnetic resonance and fluorescence correlation spectroscopy," J. Fluorescence, **18**(6), 1093-101 (2008).
[76]D.R. Lide, H.P.R. Frederikse, *CRC Handbook of Chemistry and Physics*, (77th Ed., CRC Press Inc., 1996-1997) 6-9, 6-10.; K.P. Chin, S. F. Y. Li, Y.J. Yao, L. S. Yue, " Infinite dilution coefficients of poly(ethylene glycol) and poly (propylene glycol) in water in the temperature range 303-318 K," J. Chem. Eng. Data, **36**, 329-331 (1991) ; G. Ternstrom, A. Sjostrand, G. Aly, and A. Jerqvist, " Mutual Diffusion coefficients of water + ethylene glycol and water + glycerol mixtures," J. Chem. Eng. Data, **41**, 876-879 (1996).
[77]H. Schlichting, *Boundary Layer Theory* (McGaw-Hill, Inc., New York, 1979) 90-92.
[78]F. M. White, *Viscous Flow* (McGaw-Hill, Inc., New York, 1974), 145-150.
[79]K. Ogata, *System Dynamics* (Prentice Hall, Inc., Upper Saddle River, NJ., 1998), 236-291.
[80]W. Zhang, J. Casademunt, and J. Vinals, "Study of the parametric oscillator driven by narrow-band noise to model the response of a fluid surface to time-dependent accelerations," Phys. Fluids A **5**, 3147-3161 (1993).